

Control of Doubly Fed Induction Generator based Wind Energy Conversion System

By Ramtin Golrang

November, 2012

A Thesis submitted in partial fulfillment of the requirements of

The Msc. Eng. Degree in

Electrical and Computer Engineering

Faculty of Engineering

Lakehead University

Thunder Bay, Ontario

Abstract

The doubly fed induction generator (DFIG) is widely used in today's wind energy conversion industry. The DFIG is essentially a wound rotor induction generator in which the rotor circuit can be controlled by external devices to achieve variable speed operation. This machine stands out for its flexibility and robustness, which make it an ideal device for efficient wind energy exploitation. This thesis modifies a vector-control scheme for DFIG operating as a variable-speed generator. The controller is developed in the d-q axis frame and can be used to control both active and reactive power output separately. The new speed control scheme simplifies and improves Maximum Power Point Tracking (MPPT) control over conventional PI control schemes. The machine model, control system and the modified scheme are simulated and the results are discussed. To implement the control scheme, a new position-sensorless estimation scheme for slip angular velocity is also presented in this thesis.

Acknowledgment

Foremost, I would like to express my sincere gratitude to my supervisor, Dr. Krishnamoorthy Natarajan for the continuous support of my Graduate Studies and Research, for his patience, encouragement, and immense knowledge. His guidance helped me in the research and writing of this thesis. I could not have imagined having a better advisor and mentor for my Graduate Studies.

My sincere thanks also go to Dr. Mohammed Nasir Uddin, for being my Co-supervisor for this thesis.

Last but not the least, I would like to thank my parents, for giving birth to me in the first place and supporting me spiritually through my life.

Contents

| | |
|-----------------------|------|
| Abstract..... | i |
| Acknowledgment..... | ii |
| List of Figures | vi |
| List of Tables..... | viii |
| List of Symbols | ix |

Chapter 1

| | |
|---|----------|
| Wind Power System..... | 1 |
| 1.1 Installed Wind Capacity and Growth Rate | 1 |
| 1.2 Environmental Benefits | 2 |
| 1.3 Environmental Benefits | 3 |
| 1.3.1 Visual impact..... | 3 |
| 1.3.2 Sound emissions..... | 3 |
| 1.3.3 Birds | 3 |

Chapter 2

| | |
|--|----------|
| Wind Energy Generating System | 4 |
| 2.1 Wind Turbine..... | 4 |
| 2.2 Turbine Blade..... | 6 |
| 2.3 Fixed-Speed system without Power Converter Interface | 6 |
| 2.4 Variable-Speed wind turbine systems with Reduced-Capacity Converters | 7 |
| 2.4.1 Doubly Fed Induction Generator with Rotor Converter | 8 |
| 2.5 Variable-Speed wind turbine system with Full-Capacity Power Converters | 8 |
| 2.6 Reactive Power Voltage Support..... | 9 |
| 2.7 Wind Sensor (Anemometers)..... | 10 |
| 2.8 Maximum Power Point Tracking (MPPT) Control | 11 |

Chapter 3

| | |
|--|-----------|
| Doubly Fed Induction Generator..... | 13 |
| 3.1 Space-Vector Model for Induction Machine | 14 |
| 3.2 d-q Axis Reference Frame Model..... | 16 |
| 3.3 Stator Flux Field Orientation Control of DFIG | 17 |
| 3.4 System Block Diagram | 222 |
| 3.5 Stator Flux Estimation | 233 |
| 3.6 Simulation Results | 255 |
| 3.6.1 Steady-State Analysis for DFIG WECS with MPPT Control strategy | 25 |
| 3.6.2 Power balance Calculation for DFIG WECS Simulation in Steady-State | 30 |

Chapter4

| | |
|---|-----------|
| Modified New Speed Control Scheme for Wound Rotor Induction Machine | 33 |
| 4.1 Simulation result for New Speed Control Scheme | 35 |
| 4.2 Sensorless Maximum Power Point Tracking with New Speed Control Scheme for DFIG..... | 37 |
| 4.2.1 Modified Hill Climb Search..... | 38 |
| 4.2.2 MPPT Control with the HCS Algorithm and a new Speed Control Scheme for the DFIG with Simulation Results. | 40 |

Chapter 5

| | |
|--|-----------|
| A New Rotor Position-Sensorless Estimation Scheme For DFIG..... | 43 |
| 5.1 Preliminary Computation..... | 46 |
| 5.2 Flowchart of Slip Angular Frequency Estimation | 48 |
| 5.2.1 Example..... | 49 |
| 5.3 Verification of New Position-Sensorless Estimation Scheme | 53 |
| 5.3.1 Example..... | 53 |
| 5.4 Estimation of Slip Angular Frequency with Rotor Initial position in New Position-Sensorless Scheme | 60 |
| 5.5 Simulation Result for operation of the DFIG by applying the two new schemes (Position-Sensorless estimation and new speed Control Strategy)..... | 61 |

Chapter 6

| | |
|-------------------------|-----------|
| 6.1 Conclusion | 65 |
| References | 66 |

List of Figures

| | |
|---|----|
| Fig. 1-1 Global annual cumulative installed wind power capacity [2] | 1 |
| Fig. 1-2 Top ten countries in cumulative installed wind power capacity circa 2009 [2]..... | 2 |
| Fig. 2-1 Evolution of wind turbine size (\varnothing : rotor diameter; H: tower height) [8]..... | 4 |
| Fig. 2-2 Power curve for a 2 MW wind turbine [8]..... | 5 |
| Fig. 2-3 Wind energy conversion system without power converter interface [6]. | 7 |
| Fig. 2-4 DFIG configurations with rotor converter [8]..... | 8 |
| Fig. 2-5 Variable-speed configurations with full-capacity converters [6]..... | 9 |
| Fig. 2-6 Ultrasonic anemometer wind speed sensor [8] | 10 |
| Fig. 2-7 Maximum power control with wind turbine power profile [6]..... | 11 |
| Fig. 2-8 Wind power-speed characteristics and maximum power point operation | 12 |
| Fig. 3-1 Simplified block diagram for DFIG wind energy conversion system [16]..... | 13 |
| Fig.3-2 Space-vector equivalent circuit of an induction generator in the arbitrary reference frame [14]..... | 15 |
| Fig. 3-3 Induction generator d-q axis model in the arbitrary reference frame [14]..... | 17 |
| Fig. 3-4 Space vector diagram for DFIG with stator flux oriented..... | 18 |
| Fig. 3-5 Block Diagram for DFIG WECS with stator flux oriented Control [17]..... | 22 |
| Fig. 3-6 Orientation of stator-flux in stationery reference frame..... | 23 |
| Fig. 3-7 Maximum mechanical torque..... | 26 |
| Fig. 3-8(a) q-axis rotor current and its reference | 26 |
| Fig. 3-8(b) Error of q-axis rotor current..... | 27 |
| Fig. 3-9 q-axis rotor voltage..... | 27 |
| Fig. 3-10 Rotor speed corresponded to maximum torque..... | 28 |
| Fig. 3-11 d-axis rotor voltage..... | 28 |
| Fig. 3-12(a) d-axis rotor current and its reference | 29 |
| Fig. 3-12(b) Error of d-axis rotor current..... | 29 |
| Fig. 3-13 Stator active and reactive power | 30 |
| Fig. 3-14 Power flow in DFIG wind energy conversion system | 31 |
| Fig. 4-1 Variation of k for different operating point..... | 34 |
| Fig. 4-2 Control rotor speed in generator mode..... | 36 |
| Fig. 4-3 Control rotor speed in motor mode | 37 |
| Fig. 4-4 Power curve versus rotor speed..... | 38 |
| Fig. 4-5 Power versus rotor speed..... | 39 |
| Fig. 4-6 Power versus rotor speed..... | 40 |
| Fig. 4-7 Power versus rotor speed..... | 40 |
| Fig. 4-8 MPPT with rotor speed regulation | 41 |
| Fig. 4-9 MPPT with rotor speed regulation | 42 |

| | | |
|--------------|---|----|
| Fig. 5-1 | Space vector diagram to transfer i_{abc-r} to $i_{\alpha\beta r}$ and then to i_{dq} | 44 |
| Fig. 5-2 | Space vector diagram to transfer variables from $\alpha\beta r$ to d-q or x-y frame..... | 44 |
| Fig. 5-3 | i_{dr} in d-axis (synchronous frame) and in x-axis (arbitrary reference) frame when the error is is 1.5 rad/s..... | 45 |
| Fig. 5-4 | i_{dr} in d-axis (synchronous frame) and in x-axis (arbitrary frame) when the error is 0.087 rad/s..... | 46 |
| Fig. 5-5 | Flowchart of angle estimation | 48 |
| Fig. 5-6 | Three phase rotor current | 49 |
| Fig. 5-7 | Process of slip angular frequency estimation..... | 50 |
| Fig. 5-8 | i_{dr} and i_{xr} when the error is 0.0174 rad/s..... | 51 |
| Fig. 5-9 | i_{xr} in 0.4 s when the error is 0.0174 rad/s..... | 51 |
| Fig. 5-10 | Space vector diagram to transfer v_{dqr} to $v_{\alpha\beta r}$ and then to v_{abc_r} | 52 |
| Fig. 5-11 | Rotor speed | 54 |
| Fig. 5-12 | Slip angular frequency ω_{slip} | 55 |
| Fig. 5-13 | Stationary rotor current ($i_{\alpha\beta r}$)..... | 55 |
| Fig. 5-14 | Take the sample from stationary rotor current..... | 56 |
| Fig. 5-15 | Slip angular frequency and stationary rotor current..... | 57 |
| Fig. 5-16 | Slip angular frequency, stationary rotor current and q-axis rotor current | 57 |
| Fig. 5-17 | Slip angular frequency ω_{sl} estimated in new scheme..... | 58 |
| Fig. 5-18(a) | Slip angular frequency ω_{slip} and ω_{sl} | 58 |
| Fig. 5-18(b) | Error between ω_{slip} and ω_{sl} | 59 |
| Fig. 5-19 | Slip angular frequency ω_{sl} and phase a of rotor current..... | 60 |
| Fig. 5-20 | q-axis rotor current and slip frequency ω_{sl} in new scheme | 63 |
| Fig. 5-21 | Control rotor speed in new scheme | 63 |

List of Tables

| | |
|--|----|
| Table 3-1: Induction machine parameters..... | 25 |
| Table 4-1: k_{\max} for 50 hp Induction Machine with $\omega_{r_{\max}} = 1.2\omega_s$ | 35 |

List of Symbols

| | |
|---------------------|--|
| L_s | Stator inductance |
| L_r | Rotor inductance |
| L_m | Magnetizing inductance |
| R_s | Stator resistance |
| R_r | Rotor resistance |
| i_s | Stator current |
| i_r | Rotor current |
| v_s | Stator voltage |
| v_r | Rotor voltage |
| T_e | Electromagnetic torque |
| T_m | Mechanical torque |
| λ_s | Stator flux linkage |
| λ_r | Rotor flux linkage |
| ω | Arbitrary angular frequency |
| ω_s | Grid angular frequency |
| ω_r | Rotor speed |
| ω_{slip} | Slip angular frequency |
| ω_m | Mechanical speed |
| P_s | Stator active power |
| Q_s | Stator reactive power |
| P | Number of poles |
| θ_s | Stator flux angle |
| ω_{sl} | Slip frequency by sensorless estimation |
| θ_{slip} | Slip angle by encoder's sensor |
| $\hat{\omega}_{sl}$ | Error in slip frequency by sensorless estimation |

| | |
|---------------------|---|
| γ | Angle of rotor voltage with respect to rotor axis |
| ϵ | Angle of rotor current with respect to rotor axis |
| δ | Torque angle |
| θ_r | Rotor angle |
| \bar{i}_r | Rotor current vector |
| xy | Arbitrary reference frame |
| d-q | Synchronous reference frame |
| α_r, β_r | Rotor stationary reference frame |
| α_s, β_s | Stator stationary reference frame |
| J | Moment of inertia of the rotor |
| \bar{v}_r | Rotor voltage vector |
| j | $\sqrt{-1}$ |

Chapter 1

Wind Power System

Wind power utilization is the conversion of wind energy into a useful form of energy, examples are: wind turbines to generate electricity, windmills for mechanical power, wind-pumps for water pumping or drainage, or sails to propel ship. The use of windmills to generate electricity can be traced back to the late nineteenth century with development of a 12 kW DC windmill generator [1]. It is, however, only since the 1980s that the technology has become sufficiently mature to produce electricity efficiently and reliably. Over the past two decades, a variety of wind power technologies have been developed, which have improved the conversion efficiency and reduced the cost for wind energy production. In addition to on-land installations, larger wind turbines have been pushed to offshore locations to harvest more energy and reduce their impact on land use and landscape.

1.1 Installed Wind Capacity and Growth Rate

Installed wind power capacity has been progressively growing over the last two decades. Fig. 1-1 shows the evolution of cumulative installed capacity worldwide as of 2009 [2]. The installed capacity of global wind power has increased exponentially from approximately 6 GW in 1996 to 158 GW by 2009. The wind industry has achieved an average growth rate of over 25% since 2000, and is expected to continue this trend in the coming years. This impressive growth has been spurred by the continuous cost increase of classic energy sources, cost reduction of wind turbines, governmental incentive programs, and public demand for cleaner energy resources.

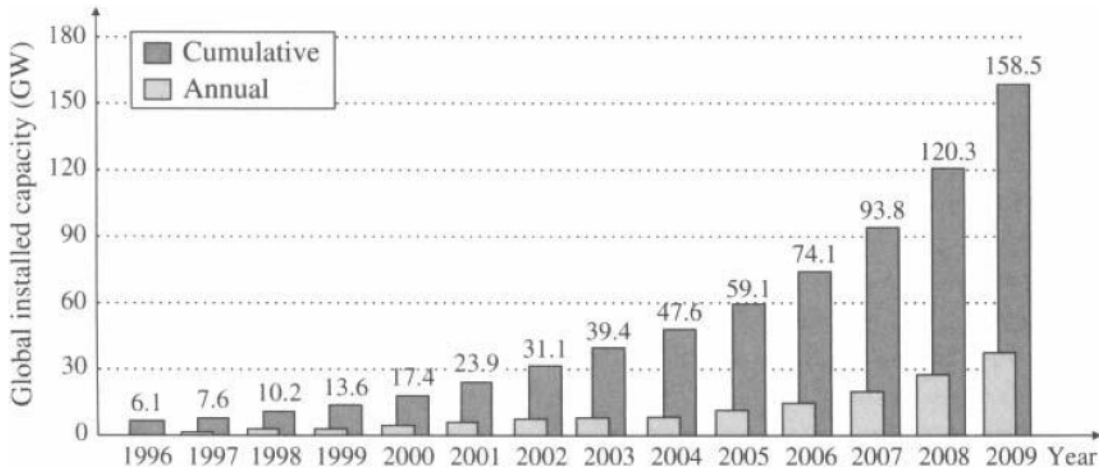


Fig. 1-1. Global annual cumulative installed wind power capacity [2]

Fig. 1-2 shows the cumulative installed wind power capacity of the top ten countries in the world as of 2009 [2]. Although Europe has maintained its role as the largest wind power producer as a region, the United States has surpassed 50% in just two years. It has circa 2009 an installed capacity of 35 GW, equivalent to 22.3% of the global installed capacity. Asian countries are catching up, mainly driven by markets in China and India. In fact, China doubled its installed capacity in one year, and is expected to continue to grow at a fast pace in the next few years.

Although this sustained growth is impressive, the real challenge is to increase the generated 6.4% of its total power demand from the wind in 2009, whereas in United States this ratio is only 1.8%. In contrast, Denmark, Portugal, and Spain lead in this aspect, with over 20%, 15% and 13% of wind power penetration, respectively.

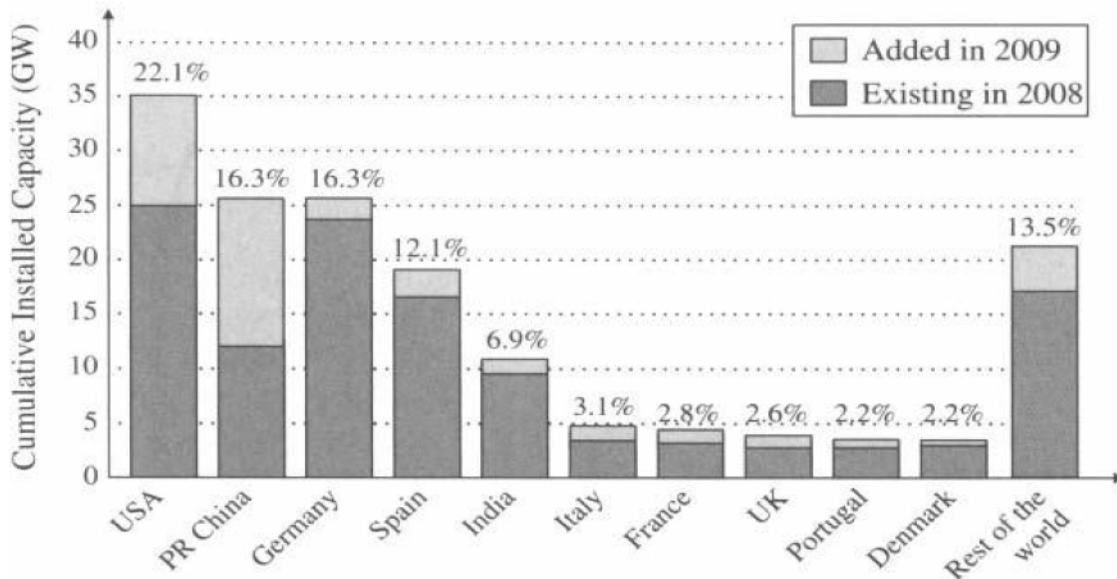


Fig. 1-2. Top ten countries in cumulative installed wind power capacity circa 2009 [2]

1.2 Environmental Benefits

Environmental pollution and the emission of CO₂ from the use of fossil fuels constitute a threat to health, the environment and sustainable economic growth. Other major pollutants from conventional power generator, which are avoided through wind power, include SO₂ and NO_x. The most serious threat comes from accelerating climate change, whose effects are already being seen around the world in rising temperatures, melting ice caps and volatile weather patterns. Climate change is direct result of the build-up of greenhouse gases in the atmosphere above the earth.

Carbon dioxide emission from power plants, industry and the transport sector are by far the largest contributor. Wind turbines cause virtually no emission during their operation and very little during their manufacture, installation, maintenance and removal. Because the fuel is free wind generated kilowatts should be used as often as possible in the electricity system to replace intermediate power loads supplied from coal and gas [3].

1.3 Environmental Impact of Wind Energy

1.3.1 Visual impact

In comparison to other energy developments, such as nuclear, coal and gas power stations or open cast coal mining, wind farms have relatively little visual impact. Nevertheless, most countries with power industry have established rules which exclude certain areas from development, such as national parks or nature reserves. Others have identified priority areas where wind power is specifically encouraged. Wind farm developers recognize that visual impact can be a concern for neighboring communities. Considerable effort is therefore committed to the planning stages in order to reduce the impact and gain their consent. Although a wind energy project can spread across a large land area, it does not occupy all that space. Farming or leisure activities can still continue around the turbines [3].

1.3.2 Sound emissions

Modern wind turbine designs have improved to the point where mechanical noise is insignificant, so the issue is now aerodynamic noise from the turbine blades. At a distance of 300 meters from a 1 MW wind turbine, the expected sound level is deemed 'quiet' and the noise from turbines is usually masked by other ambient sounds such as the movement of trees when the wind picks up, or near an industrial or urban area [4].

1.3.3 Birds

Collisions of birds with turbines have been an issue at some older wind farm sites from the 1980s, especially the Altamont Pass in California- a result of poor setting, out-moded turbines and tower technology. Subsequent experiences in Germany and Denmark show that such effects can be avoided by responsible planning practice. Proper installation of turbines is important if adverse impacts are to be avoided. In the United States, a study in 2001 estimated fatalities for each turbine. By comparison, between 100 and 1,000 million birds are estimated to die each year in US from colliding with vehicles, buildings, power lines and other structures [5].

Chapter 2

Wind Energy Generating System

As shown in Fig. 2-1, wind energy technology has evolved rapidly over the last decades with increasing rotor diameters and the use of sophisticated power electronics to allow operation at variable rotor speed [8].

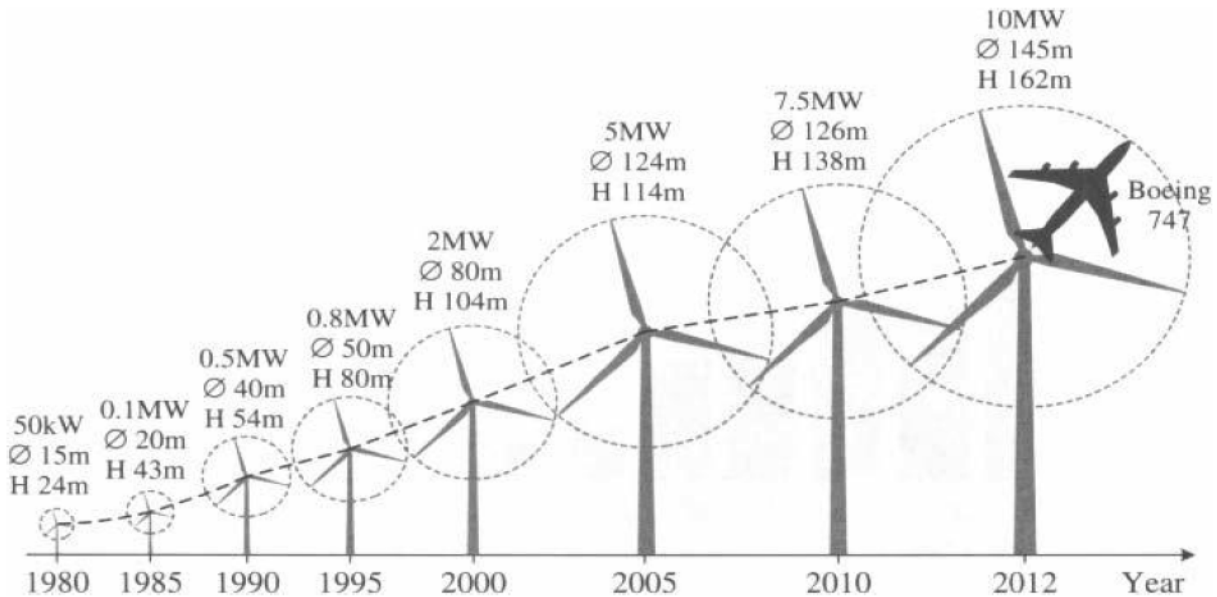


Fig. 2-1. Evolution of wind turbine size (\varnothing : rotor diameter; H: tower height) [8]

2.1 Wind Turbine

Wind turbines produce electricity by using the power of the wind to drive an electricity generator. Wind passes over the blades, generating lift and exerting force. The rotating blades turn a shaft inside the nacelle, which goes into a gearbox. The gearbox increases the rotational speed to that which is appropriate for the generator, which uses magnetic fields to convert the rotational energy into electrical energy.

The power output of a wind turbine at various wind speed is conventionally described by its power curve [8]. The power curve gives the steady-state electrical power output as a function of the wind speed. An example of power curve is given in Fig. 2-2 for 2 MW wind turbine.

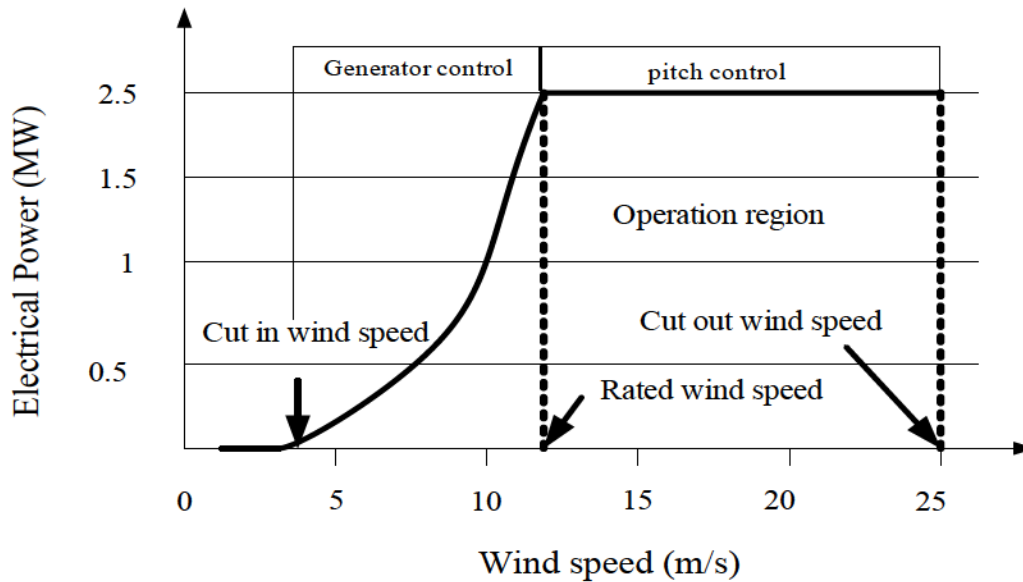


Fig. 2-2. Power curve for a 2 MW wind turbine [8]

The power curve has three key points on the velocity scale:

- Cut-in wind speed—the minimum wind speed at which the machine will deliver useful power.
- Rated wind speed—the wind speed at which rated power is obtained (rated power is generally the maximum power output of the generator).
- Cut-out wind speed—the maximum wind speed at which the turbine is allowed to deliver power (usually limited by engineering loads and safety constraints).

The rated wind speed is the speed at which the system produces nominal power, which is also the rated output power of the generator. The cut-out wind speed is the highest wind speed at which the turbine is allowed to operate before it is shut down.

For wind speed above the cut-out speed, the turbine must be stopped to prevent damage from excessive wind. To deliver captured power to the grid at different wind speeds, the wind generator should be properly controlled with variable speed operation. As the wind speed increases beyond the rated speed, aerodynamic power control of blades is required to keep the power at the rated value [6, 7].

2.2 Turbine blade

The blade is the distinctive and visible component of a wind turbine. It is also responsible for carrying out of the most essential task of the energy conversion process: transforming the wind kinetic energy into rotational mechanical energy. Single- and two-blade wind turbines have found practical applications, the three-blade rotor is considered the industry standard for large wind turbines. Turbines with fewer blades operate at higher rotational speeds. This is an advantage from the drive train point of view since they require a gearbox with a lower gear ratio, which translates into lower cost. In addition fewer blades imply lower costs. However, acoustic noise increases proportionally to the blade tip speed. Therefore, acoustic noise is considerably higher for single-and two-blade turbines, which is considered an important problem, particularly in populated areas. Single-blade turbines have an asymmetrical mechanical load distribution. The turbine rotors are aerodynamically unbalanced, which can cause mechanical vibrations.

Rotors with more than three blades are not common since they are more expensive. Operating at lower rotational speed requires a higher gear ratio. The lagging wind turbulence of one blade can affect the other blades since they are closer to each other. Hence, the three-blade rotor presents the best trade-off between mechanical stress, acoustic noise, cost and rotational speed for large wind turbines [8].

2.3 Fixed-Speed system without Power Converter Interface

In [6, 7], a typical configuration of wind energy conversion system (WECS) without a power converter interface is illustrated in Fig. 2-3, where the generator is connected to the grid through a transformer. A squirrel cage induction generator (SCIG) is exclusively used in this type of WECS, and its rotational speed is determined by the grid frequency and the number of poles of the stator winding. For a four-pole 1 MW generator connected to a grid of 60 Hz, the generator operates at a speed slightly higher than 1800 rpm. At different wind speeds, the generator speed varies within 1% of its rated speed.

The speed range of the generator is so small that this system is often known as a fixed- speed WECS, as mentioned earlier. A gearbox is normally required to match the speed difference between the turbine and generator such that the generator can deliver its rated power at the rated wind speed. This configuration requires a soft starter to limit high inrush currents during system start-up, but the soft starter is bypassed by switch after the system is started. A three- phase capacitor bank is usually required to compensate for the reactive power drawn by the induction generator. This wind energy system features simplicity, low maintenance costs, and reliable operation. The main drawbacks include: (1) the system delivers the rated power to the grid only at

a given wind speed, leading to low energy conversion efficiency at other wind speeds; and (2) the power delivered to the grid fluctuates with the wind speed, causing disturbances to the grid.

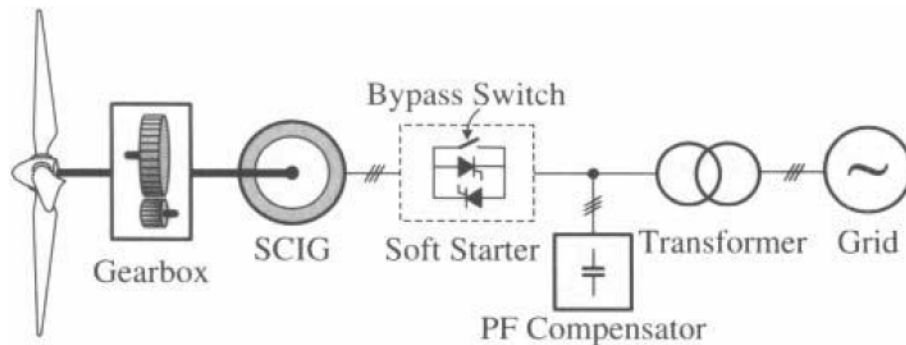


Fig. 2-3. Wind energy conversion system without power converter interface [6]

2.4 Variable-Speed wind turbine systems with Reduced-Capacity Converters

Variable-speed operation has a number of advantages over fixed-speed wind systems. It increases the energy conversion efficiency and reduces mechanical stress caused by wind gusts. The latter has a positive impact on the design of the structure and mechanical parts of the turbine and enables the construction of larger wind turbines. It also reduces the wear and tear on the gearbox and bearings, expanding the life cycle and reducing the maintenance requirements.

The main drawback of variable-speed WECS is the need for a power converter interface to control the generator speed, which adds cost and complexity to the system. However, the power converter decouples the generator from the grid, which enables the control of the grid-side active and reactive power. Variable-speed WECS can be further divided into two types based on the power rating of the converter with respect to the total power of the system: reduced-capacity power converter and full-capacity power converter. The variable-speed WECS with reduced-capacity converters are only feasible with wound-rotor induction generators (WRIG) since variable-speed operation can be achieved by controlling the rotor currents without the need to process the total power of the system [6].

2.4.1 Doubly Fed Induction Generator with Rotor Converter

A typical diagram of the doubly fed induction generator (DFIG) wind energy system is shown in Fig. 2-4. The configuration of this system shows that the rotor circuit is connected to the grid by power converter system, and in this system the power factor can be adjusted by the power converter. The converters only have to process the slip power in the rotor circuits, which is approximately 30% of the rated power of the generator, resulting in reduced converter cost in comparison to the wind energy systems using full-capacity converters [9, 10]. The use of converters also allows bidirectional power flow in the rotor circuit and increases the speed range of the generator. This system features improved overall power conversion efficiency, extended generator speed range ($\pm 30\%$), and enhanced dynamic performance as compared to the fixed speed WECS. These features have made the DFIG wind energy system widely accepted in today's market.

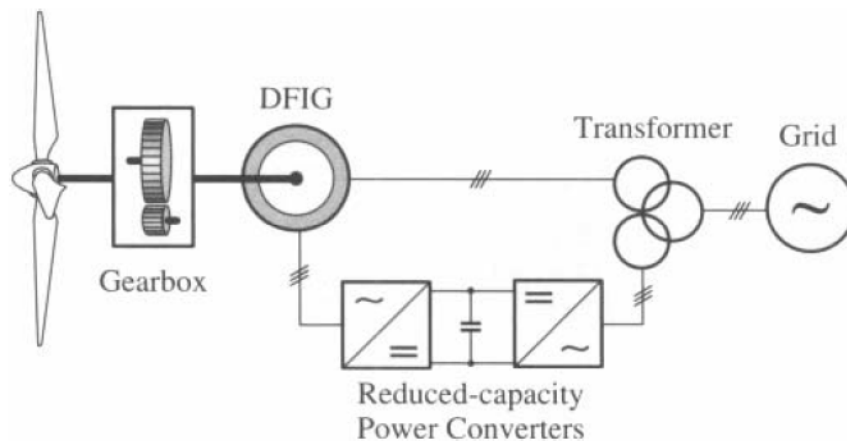


Fig. 2-4. DFIG configurations with rotor converter [6]

2.5 Variable-Speed wind turbine system with full capacity power converters

The performance of the wind energy system can be greatly enhanced with the use of a full-capacity power converter. Fig. 2-5 shows such a system in which the generator is connected to the grid via a full-capacity converter system. Squirrel cage induction generator, wound rotor synchronous generator, and permanent magnet synchronous generator (PMSG) have all found applications in this type of configuration. The power rating of the converter is normally the same as that of the generator. With the use of the power converter, the generator is fully decoupled from the grid, and

can operate in full speed range. This also enables the system to perform reactive power compensation and smooth the grid connection. The main drawback is a more complex system with increased costs. It is noted that the wind energy system can operate without the need for a gearbox if a low-speed synchronous generator with a large number of poles is used. The elimination of the gearbox improves the efficiency of the system and reduces initial costs and maintenance. However, a low-speed generator has a substantially larger diameter to accommodate the large number of poles on the perimeter, which may lead to an increase in generator size [6].

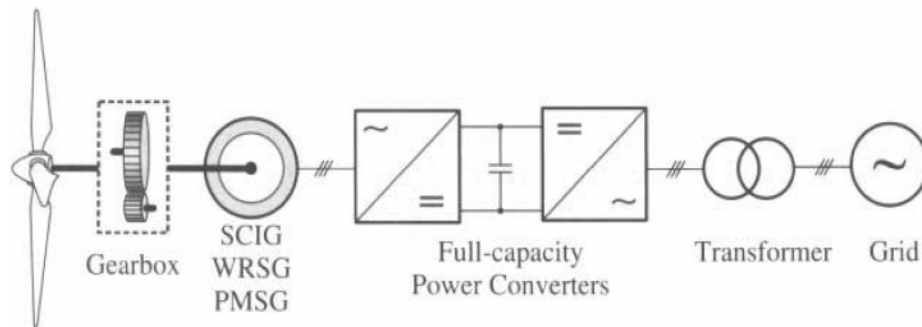


Fig. 2-5. Variable-speed configurations with full-capacity converters [6]

2.6 Reactive Power Voltage Support

Fixed-speed induction generators absorb reactive power to maintain their magnetic field and have no direct control over their reactive power flow. Therefore, in the case of fixed-speed induction generator, the only way to support the voltage of the network is to reduce the reactive power drawn from the network by the use of shunt compensators. Variable-speed wind turbines have the capability of reactive power control and may be able to support the voltage of the network to which they are connected. However, individual control of wind turbines may not be able to control the voltage at the point of connection, especially because the wind farm network is predominantly inductive. On many occasions, the reactive power and voltage control at the point of connection of the wind farm is achieved by using reactive power compensation equipment such as static Var compensators (SVCs) or static synchronous compensators (STATCOMs) [7, 13].

2.7 Wind Sensor (Anemometers)

The yaw control system of the turbine allows the turbine to be oriented into the wind direction for maximum wind capture. In addition, in variable speed turbines, the wind speed measurement is needed to determine the generator speed for maximum power extraction. Most large wind turbines are equipped with sensors, also referred to as anemometers, for wind data collection and processing. The wind speed sensor is usually made of a three-cup vertical-axis micro-turbine driving an optoelectronic angle transducer. These are the main components of a wind measurement system, and are usually located on the top back part of the nacelle. More than one sensor system may be used in a wind turbine for more reliable and accurate measurements. Ultrasonic anemometers are also used in practical wind turbines. They measure the wind speed by emitting and receiving acoustic signals through the air and monitoring the transmission time. Several emitters and receptors are disposed in such a way that a three-dimensional measurement can be made. The transmission time is affected by both wind speed and direction. With a given physical distribution of the sensors, the wind speed and direction can be computed from the propagation time. The ultrasonic anemometers are more accurate and reliable than mechanical ones with moving parts. However, they are more expensive. Fig. 2-6 shows an ultrasonic anemometer on the top of the nacelle of a modern wind turbine [8].



Fig. 2-6. Ultrasonic anemometer wind speed sensor [8]

2.8 Maximum Power Point Tracking (MPPT) Control

Variable- speed wind generation systems are more attractive than fixed-speed system because of the more efficient energy production, improved power quality and improved dynamic performance during grid disturbances. By adjusting the shaft speed optimally, the variable-speed wind turbine generators (WTGs) can achieve the maximum wind power generation at various wind speed within the operating range. To implement maximum wind power extraction, most controller designs of the variable-speed WTGs employ anemometers to measure wind speed in order to derive the desired optimal shaft speed for adjusting the generator speed. In most cases, a number of anemometers are placed surrounding the wind turbine at some distance to provide adequate wind speed information [6].

In Fig. 2-7, the wind speed is measured in real time by a wind speed sensor. According to the MPPT profile provided by the manufacturer, the power reference P_m^* is generated and sent to the generator control system, which compares the power reference with the measured power P_m from the generator to produce the control signals for the power converter. Through the control of power converters and generator (indirectly), the mechanical power P_m of the generator will be close to its reference in steady state, at which the maximum power operation is achieved.

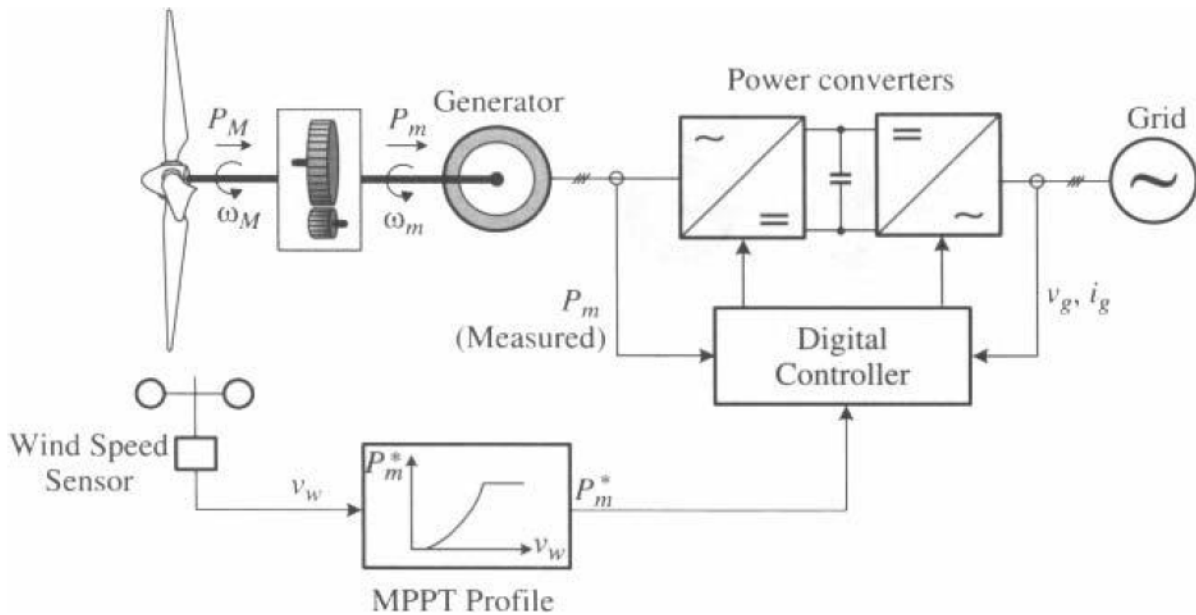


Fig. 2-7. Maximum power control with wind turbine power profile [6]

Through the control of power converters and thereby the generator, the mechanical power P_m of the generator will be closed to its reference in steady state, at which the maximum power operation is achieved. It is noted that the power losses of the gearbox and drive train in the above analyses are neglected and, therefore, the mechanical power of the generator P_m is equal to the mechanical power P_M produced by the turbine [11, 12]. When the wind speed is above the cut-in wind speed and below the rated wind speed, maximum power point tracking strategy is used to extract the available power from the wind turbine. Fig. 2-8 shows the power characteristics of wind turbine.

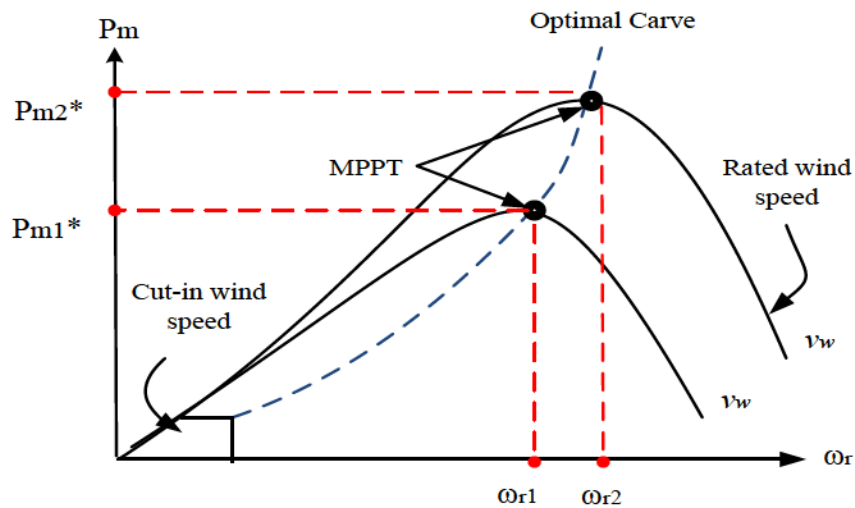


Fig. 2-8. Wind power-speed characteristics and maximum power point operation

A typical relationship, as shown in Fig. 2-8, indicates that there is one rotor electrical speed at which the wind turbine is most efficient under specific wind speed. Hence, to achieve maximum power point, the rotor speed (ω_r) should be regulated to keep the tip speed-ratio at the optimal operating point for all wind speeds.

Chapter 3

Doubly Fed Induction Generator

A typical configuration of a DFIG wind turbine is shown in Fig. 3-1. It uses a wound rotor induction generator with slip-rings to transmit current between the converter and the rotor windings and variable-speed operation is obtained by injecting a controllable voltage into the rotor at the desired slip frequency. The rotor winding is fed through a variable-frequency power converter, typically based on two AC/DC IGBT- based voltage source converters (VSCs) and linked through a DC bus. The variable-frequency rotor supply from the converter enables the rotor mechanical speed to be decoupled from the synchronous frequency of the electrical network, thereby allowing variable-speed operation of the wind turbine.

A DFIG wind turbine can transmit power to the network through both the generator stator and the converters. When the generator operates in super-synchronous mode, power will be delivered from the rotor through the converters to the network, and when the generator operates in sub-synchronous mode, the rotor will absorb power from the network through the converters [6].

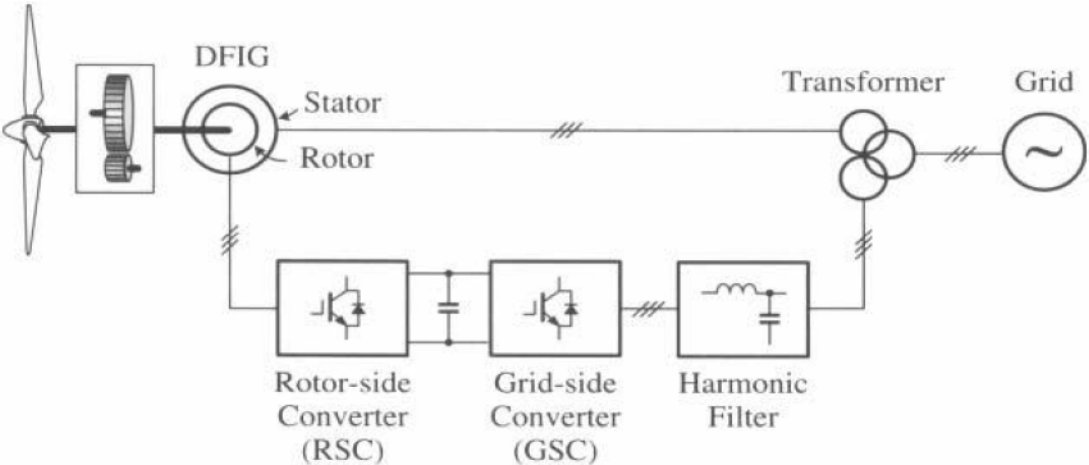


Fig. 3-1. Simplified block diagram for DFIG wind energy conversion system [6]

3.1 Space-Vector Model for Induction Machine

In [6, 14], the induction generator (IG) space-vector model is generally composed of three sets of equations: voltage equations, flux linkage equations, and equation of motion. The voltage equations for the stator and rotor of the generator in an arbitrary reference frame are given by

$$v_s = R_s i_s + \frac{d\lambda_s}{dt} + j\omega\lambda_s \quad (3.1)$$

$$v_r = R_r i_r + \frac{d\lambda_r}{dt} + j(\omega - \omega_r)\lambda_r \quad (3.2)$$

The terms $j\omega\lambda_s$ and $j(\omega - \omega_r)\lambda_r$ on the right-hand side of (3.1) and (3.2) are referred to as speed voltages, which are induced by the rotation of the reference frame at the arbitrary speed of ω . The second set of equations is for the stator and rotor flux linkages λ_s and λ_r .

$$\lambda_s = (L_{ls} + L_m)i_s + L_m i_r = L_s i_s + L_m i_r \quad (3.3)$$

$$\lambda_r = (L_{lr} + L_m)i_r + L_m i_s = L_r i_r + L_m i_s \quad (3.4)$$

All the rotor-side parameters and variables, such as R_r , L_{lr} , λ_r in the above equations are referred to the stator side.

The third and final equation is the equation of motion, which describes the dynamic behavior of the rotor mechanical speed in terms of mechanical and electromagnetic torque [6]:

$$J \frac{d\omega}{dt} = T_e - T_m \quad (3.5)$$

$$T_e = \frac{3P}{2} \operatorname{Re}(j\lambda_s i_s^*) = -\frac{3P}{2} \operatorname{Re}(j\lambda_r i_r^*) \quad (3.6)$$

The above equations constitute the space-vector model of the induction generator, whose equivalent circuit representation is given in Fig. 3-2. The generator model is in the arbitrary reference frame, rotating in space at the arbitrary speed ω .

The space-vector model and its associated equations can be used to model the induction machine either as a motor or a generator. The induction generator model of Fig. 3-2 in the arbitrary reference frame can be easily transformed into the other reference frames. For example, a synchronous frame model is very useful for simulation and digital implementation of IG WECS with advanced control systems. Such a model can be obtained by setting the arbitrary speed ω in (3.1) and (3.2) and in Fig. 3-2 to the synchronous speed ω_s .

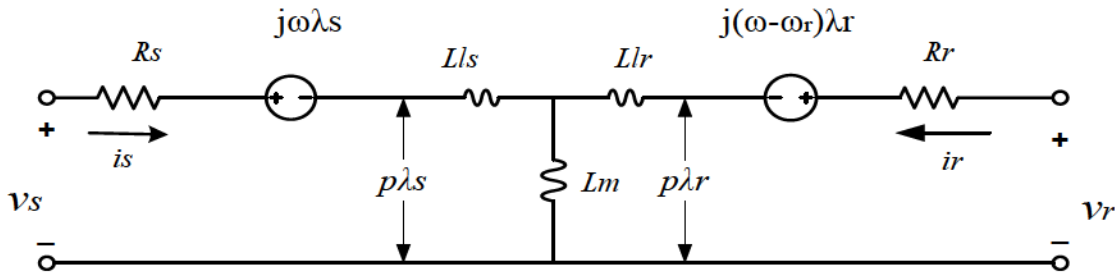


Fig. 3-2. Space-vector equivalent circuit of an induction generator in an arbitrary reference frame [14]

The derived model in the synchronous frame is given in Fig. 3-2, with $\omega = \omega_s$ is the synchronous speed and ω_{slip} is the angular slip frequency of the generator, given by

$$\omega_s = 2\pi f_s \quad (3.7)$$

$$\omega_{slip} = \omega_s - \omega_r \quad (3.8)$$

The synchronous speed of the reference frame ω_s corresponds to the stator angular frequency, which is proportional to the stator frequency f_s .

To obtain the induction generator (IG) model in the stationary reference frame, we can set the speed of the arbitrary frame ω in Fig. 3-2 to zero since the stationary frame does not rotate in space.

The IG space-vector models in Fig. 3-2 (and Fig. 3-3) are valid for both SCIG and DFIG. In the SCIG, the rotor circuit is shorted and, therefore, the rotor voltage is set to zero, whereas for the DFIG the rotor circuit is connected to a power converter system that controls the speed and torque of the generator.

3.2 d-q Axis Reference Frame Model

In [14], the d-q axis model of the induction generator can be obtained by decomposing the space-vectors into their corresponding d-q axis components, that is,

$$v_s = v_{ds} + jv_{qs}; i_s = i_{ds} + ji_{qs}; \lambda_s = \lambda_{ds} + j\lambda_{qs} \quad (3.9)$$

$$v_r = v_{dr} + jv_{qr}; i_r = i_{dr} + ji_{qr}; \lambda_r = \lambda_{dr} + j\lambda_{qr} \quad (3.10)$$

Substituting (3.9) and (3.10) into (3.1) and (3.2) and grouping real and imaginary components on both sides of the equations, the d-q axis voltage equations for the induction generator are obtained:

$$v_{ds} = R_s i_{ds} + \frac{d\lambda_{ds}}{dt} - \omega \lambda_{qs} \quad (3.11)$$

$$v_{qs} = R_s i_{qs} + \frac{d\lambda_{qs}}{dt} + \omega \lambda_{ds} \quad (3.12)$$

$$v_{dr} = R_r i_{dr} + \frac{d\lambda_{dr}}{dt} - (\omega - \omega_r) \lambda_{qr} \quad (3.13)$$

$$v_{qr} = R_r i_{qr} + \frac{d\lambda_{qr}}{dt} + (\omega - \omega_r) \lambda_{dr} \quad (3.14)$$

Similarly, substituting (3.9) and (3.10) into (3.3) and (3.4), the d-q axis flux linkages are obtained:

$$\lambda_{ds} = L_s i_{ds} + L_m i_{dr} \quad (3.15)$$

$$\lambda_{qs} = L_s i_{qs} + L_m i_{qr} \quad (3.16)$$

$$\lambda_{dr} = L_r i_{dr} + L_m i_{ds} \quad (3.17)$$

$$\lambda_{qr} = L_r i_{qr} + L_m i_{qs} \quad (3.18)$$

The electromagnetic torque T_e in (3.6) can be expressed by d-q axis flux linkages and currents as well. By mathematical manipulations, several expressions for the torque can be obtained. The most commonly used expressions are given by

$$T_e = \frac{3}{2} P (\lambda_{ds} i_{qs} - \lambda_{qs} i_{ds}) \quad (3.19)$$

$$T_e = \frac{3}{2L_r} L_m P (\lambda_{dr} i_{qs} - \lambda_{qr} i_{ds}) \quad (3.20)$$

$$T_e = \frac{3}{2} L_m P (i_{dr} i_{qs} - i_{qr} i_{ds}) \quad (3.21)$$

(3.11) to (3.21) represent the d-q axis model of the induction generator in the arbitrary reference frame, and its corresponding d-q axis equivalent circuits are shown in Fig. 3-3.

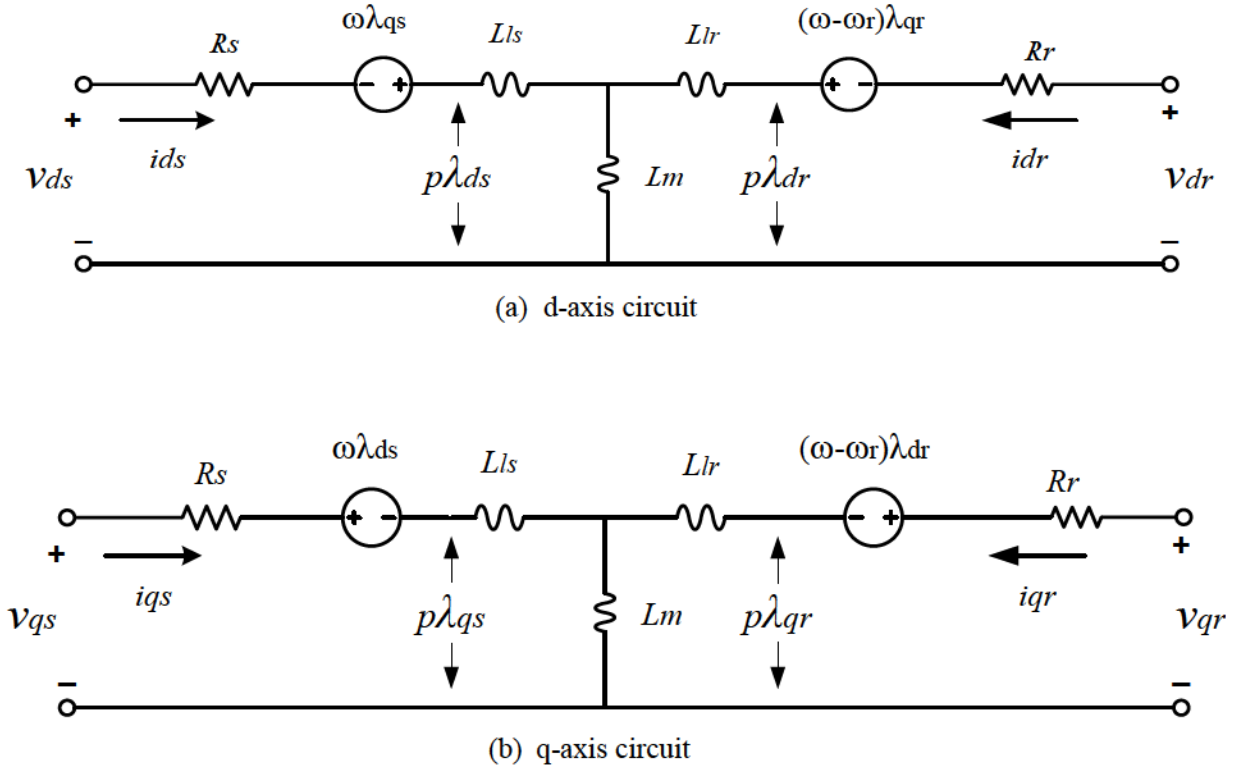


Fig. 3-3. Induction generator d-q axis model in an arbitrary reference frame [14]

To obtain the d-q axis model in the synchronous or stationary reference frames, the speed of the arbitrary reference frame ω can be set to the synchronous (stator) frequency ω_s of the generator or zero, respectively.

3.3 Stator Flux Field Orientation Control of DFIG

The general control technique of a DFIG is the decoupled d-q control approach in the synchronous frame that uses the rotor quadrature axis current i_{qr} for real power control and rotor direct axis current i_{dr} for reactive power control [9, 15- 17].

In the above equations, f can represent either voltage or current and flux linkage. The rotating speed of the synchronous reference frame is given by

$$\omega_s = 2\pi f_s \quad (3.26)$$

Where f_s is the stator frequency of the generator (also the frequency of the grid voltage). The stator flux vector angle θ_s is referenced to the stator frame, which varies from zero to 2π when λ_s rotates one revolution in space. The rotor rotates at speed ω_r . The rotor position angle θ_r is also referenced to the stator frame.

The angle δ in Fig. 3-4 is an angle between stator flux λ_s and rotor flux λ_r , which is called torque angle [14]. The three phase rotor currents are a function of $\epsilon(t)$ for balanced system, therefore the ϵ is a rotor vector angle with respect to the rotor axis.

The angle between stator flux vector and the rotor axis is called slip angle, and defined by

$$\theta_{slip} = \theta_s - \theta_r \quad (3.27)$$

The slip angle can be derived either from position encoder sensor or with sensorless estimation method, in this chapter slip angle obtained from encoder sensor. In chapter five a new position-sensorless scheme for slip angular velocity will be developed.

The flux linkages of stator and rotor in d-q axis synchronous reference frame will be:

$$\lambda_{ds} = L_s i_{ds} + L_m i_{dr} \quad (3.28)$$

$$\lambda_{qs} = L_s i_{qs} + L_m i_{qr} \quad (3.29)$$

$$\lambda_{dr} = L_r i_{dr} + L_m i_{ds} \quad (3.30)$$

$$\lambda_{qr} = L_r i_{qr} + L_m i_{qs} \quad (3.31)$$

And stator and rotor voltage in d-q axis synchronous reference frame can be shown as:

$$v_{ds} = R_s i_{ds} + \frac{d\lambda_{ds}}{dt} - \omega_s \lambda_{qs} \quad (3.32)$$

$$v_{qs} = R_s i_{qs} + \frac{d\lambda_{qs}}{dt} + \omega_s \lambda_{ds} \quad (3.33)$$

$$v_{dr} = R_r i_{dr} + \frac{d\lambda_{dr}}{dt} - (\omega_s - \omega_r) \lambda_{qr} \quad (3.34)$$

$$v_{qr} = R_r i_{qr} + \frac{d\lambda_{qr}}{dt} + (\omega_s - \omega_r) \lambda_{dr} \quad (3.35)$$

The stator voltage in d-axis and q-axis are

$$v_{ds} = 0 \text{ and } v_{qs} = v_s \quad (3.36)$$

Where v_s is a rms magnitude of three phase stator voltage

If the stator flux is aligned with d-axis in the synchronous rotating reference frame, then $\lambda_{qs} = 0$ and by substituting (3.29), and with $\lambda_{ds} = \lambda_s = L_m i_{ms}$ where i_{ms} is the magnetizing current in (3.28), the stator currents components can be shown as:

$$\lambda_{qs} = 0 = L_s i_{qs} + L_m i_{qr} \Rightarrow i_{qs} = -\frac{L_m}{L_s} i_{qr} \quad (3.37)$$

$$\lambda_{ds} = L_s i_{ds} + L_m i_{dr} \Rightarrow i_{ds} = -\frac{L_m}{L_s} i_{dr} + \frac{L_m}{L_s} |i_{ms}| \quad (3.38)$$

Now, substituting these current components in the electromagnetic torque given by (3.19), the electrical torque becomes

$$T_e = \frac{3}{2} L_m P (\lambda_{ds} i_{qs}) = -\frac{3}{2} L_m P \left(\lambda_{ds} \frac{L_m}{L_s} \right) i_{qr} \quad (3.39)$$

Active and reactive power equations can be obtained by substituting (3.37), (3.38) into (3.40) and (3.41).

$$P_s = 1.5 * (v_{ds} i_{ds} + v_{qs} i_{qs}) \quad (3.40)$$

$$Q_s = 1.5 * (v_{qs} i_{ds} - v_{ds} i_{qs}) \quad (3.41)$$

Thus:

The stator real and reactive powers are:

$$P_s = -1.5 * v_s \left(\frac{L_m}{L_s} \right) i_{qr} \quad (3.42)$$

$$Q_s = 1.5 * v_s \frac{L_m}{L_s} (|i_{ms}| - i_{dr}) \quad (3.43)$$

Equations (3.39), (3.42) and (3.43) indicate that T_e , P_s and Q_s can be controlled independently by regulating the rotor current components, i_{qr} and i_{dr} , respectively in stator flux oriented scheme.

To properly control the machine, it is possible to set the relationship between the rotor currents and voltage applied to the rotor [17, 18].

$$v_{dr} = R_r i_{dr} + \sigma L_r p i_{dr} - \omega_{slip} \sigma L_r i_{qr} \quad (3.44)$$

$$v_{qr} = R_r i_{qr} + \sigma L_r p i_{qr} + \omega_{slip} \left(\frac{L_m^2}{L_s} i_{ms} + \sigma L_r i_{dr} \right) \quad (3.45)$$

Where p is differential operation: d/dt and $\sigma = \left(1 - \frac{L_m^2}{L_r L_s}\right)$, $\lambda_{dr} = \frac{i_{ms} L_m^2}{L_s}$.

Equations (3.44) and (3.45) indicates that i_{dr} and i_{qr} respond to v_{dr} and v_{qr} respectively, through a first-order transfer function with simple cross-coupling. It is therefore possible to design the following feedback decoupling loops and PI controllers [17, 18].

$$v_{dr} = \left(k_{pr} + \frac{k_{ir}}{s} \right) (i_{dr}^* - i_{dr}) - \omega_{slip} \sigma L_r i_{qr} \quad (3.46)$$

$$v_{qr} = \left(k_{pr} + \frac{k_{ir}}{s} \right) (i_{qr}^* - i_{qr}) + \omega_{slip} \left(\frac{L_m^2}{L_s} i_{ms} + \sigma L_r i_{dr} \right) \quad (3.47)$$

3.4 System Block Diagram for DFIG Control with Stator Flux Oriented

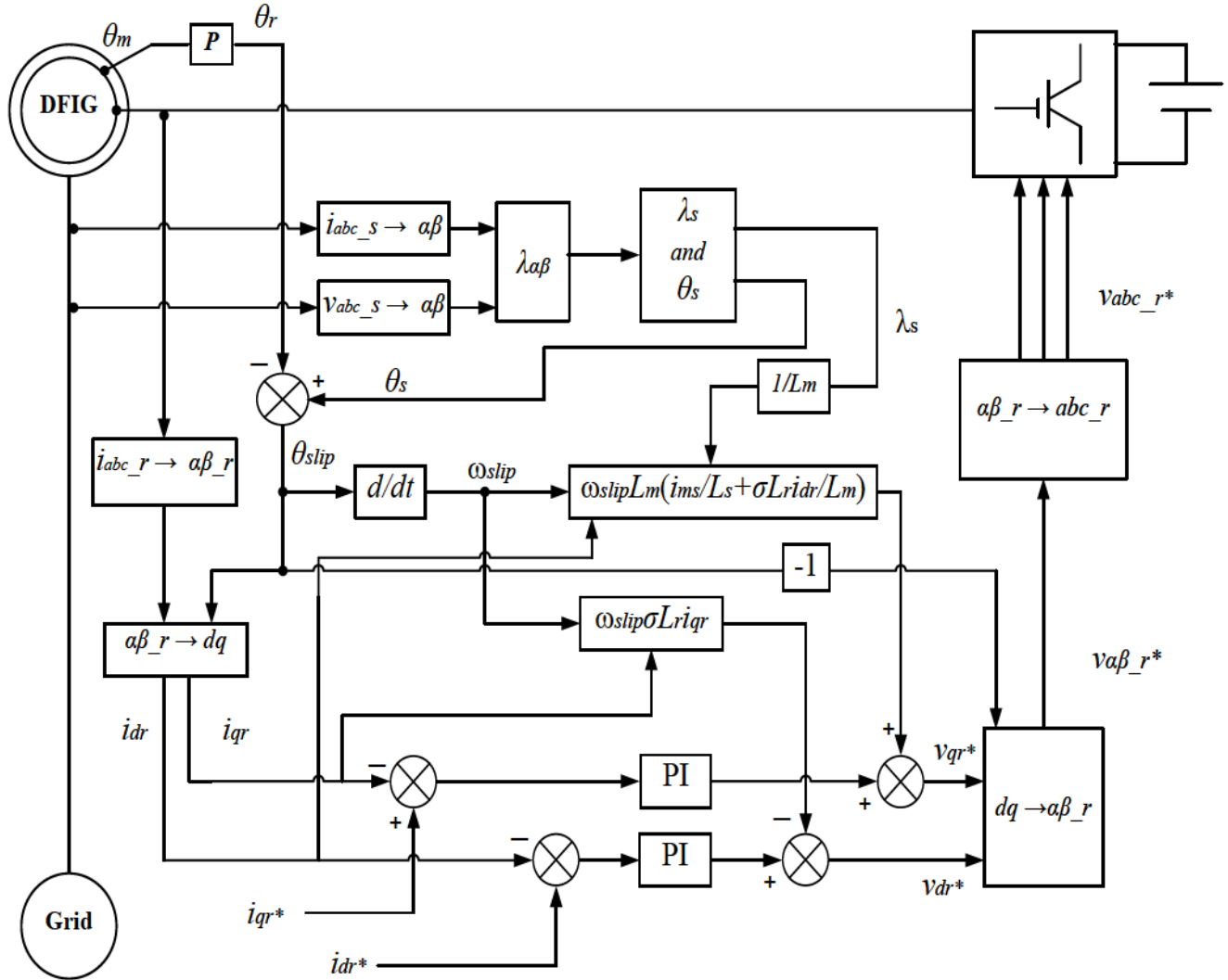


Fig. 3-5. Block diagram for DFIG WECS with stator flux oriented control [17]

Fig. 3-5 shows the block diagram of DFIG wind energy system with stator flux oriented control. The stator flux angle is identified by the θ_s calculator, and the rotor position angle θ_r is measured by an encoder mounted on the shaft of the generator.

The slip angle for the reference frame transformation is obtained by $\theta_{slip} = \theta_s - \theta_r$. The stator variables will be transferred from three phase abc_s frame to $\alpha\beta_s$ stationary reference frame and from $\alpha\beta_s$ to the d-q axis synchronous reference frame, and vice versa. The angle of the stator flux vector can be obtained by stator flux estimation.

The MPPT block generates the reference torque T_e^* based on the optimal torque method discussed in Section 2.8 for maximum power point tracking.

The reference for the q -axis rotor current i_{qr}^* which is the torque producing component of the rotor current is calculated according to (3.39). For a given stator reactive power reference Q_s^* the d-axis rotor current reference i_{dr}^* is calculated by (3.43). The reference d-q axis currents, i_{qr}^* and i_{dr}^* , are then compared to the measured values, i_{dr} and i_{qr} and the errors passed through PI controllers.

The output of the PI controllers, v_{dr}^* and v_{qr}^* are the d-q axis rotor voltage references in the synchronous frame, which are transformed into a two-phase stationary reference $v_{\alpha r}^*, v_{\beta r}^*$ and then transferred to three phase rotor voltages, v_{ar}^*, v_{br}^* , and v_{cr}^* . The rotor reference voltages can serve as the three-phase modulating waveforms in carrier-based modulation schemes or be converted into a reference space vector for the space vector modulation (SVM) [15, 17].

The PWM block generates gating signals for the rotor-side converter. The main function of grid converter is to keep the DC link voltage V-DC constant. The overall power factor of the DFIG wind energy system is then controlled by the rotor-side converter through its reference Q_s^* .

3.5 Stator Flux Estimation

The stator flux estimation based on the voltage model is determined from the stator voltage equation [19, 20] given by:

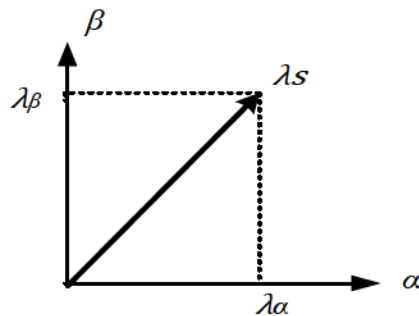


Fig. 3-6. Orientation of stator-flux in stationary reference frame

$$\lambda_{\alpha s} = \int (v_{qs} - R_s i_{qs}) dt \quad (3.48)$$

$$\lambda_{\beta s} = \int (v_{ds} - R_s i_{ds}) dt \quad (3.49)$$

The flux angle can be expressed as:

$$\theta_s = \tan^{-1} \frac{\lambda_{\beta s}}{\lambda_{\alpha s}} \quad (3.50)$$

And the synchronous angular velocity is estimated by derivative of θ_s , $\omega_s = \frac{d\theta_s}{dt}$.

$$|\lambda_s| = \sqrt{\lambda_{\alpha s}^2 + \lambda_{\beta s}^2} \quad (3.51)$$

$$\omega_s = \frac{d\theta_s}{dt} \quad (3.52)$$

$$\omega_s = \frac{\lambda_{\alpha s} p \lambda_{\beta s} + \lambda_{\beta s} p \lambda_{\alpha s}}{\lambda_{\alpha s}^2 + \lambda_{\beta s}^2} \quad (3.53)$$

Where p is differential operator.

3.6 Simulation Results

Simulation of the proposed control strategy for a DFIG based generation system is carried out in MATLAB. Fig. 2-4 shows the schematic of the implemented system. The parameters of the machine are from [14], and given here in Table 3-1. In Table 3-1 the voltage is the rated rms line-to-line voltage, the speed is rated speed, and J includes the inertia of the load which is assumed to be equal to rotor of machine and turbine rotor.

| Hp | volts | rpm | T_B N m | i_{abc} A | r_s Ω | X_{ls} Ω | X_M Ω | X_{lr} Ω | r_r Ω | J kg m ² | Pole |
|----|-------|------|--------------|----------------|-------------------|----------------------|-------------------|----------------------|-------------------|--------------------------|------|
| 50 | 460 | 1705 | 198 | 46.8 | 0.087 | 0.302 | 13.08 | 0.302 | 0.228 | 1.662 | 4 |

Table. 3-1. Induction machine parameters

Based on the proposed Stator-flux Oriented Control (SFOC) strategy, the rotor-side converter controls the DFIG stator's active and reactive power. The dynamic performance of DFIG WECS with stator-flux oriented control is analyzed in the following sub-sections.

3.6.1 Steady state Analysis for DFIG WECS with MPPT Control strategy

This sub-section analyzes the performance of the DFIG based on maximum power point tracking (MPPT) in steady-state, and also shows that the reactive power can be controlled by adjusting the d-axis of rotor current (i_{dr}).

The ensuing simulation shows the DFIG operation controlling reactive power and extracting maximum active power from the wind turbine at two operating points with the controls of Section 3.4 and 3.5.

In Fig. 3-7 the maximum input mechanical torque between $2.5 \text{ s} \leq t \leq 8 \text{ s}$ is $T_{mB} = 150 \text{ Nm}$, and between $8 \text{ s} \leq t \leq 14 \text{ s}$ is $T_{mA} = 250 \text{ Nm}$, and for reactive power control: $i_{dr}^* = 0 \text{ A}$ between $0 \leq t \leq 2.5 \text{ s}$ and $i_{dr}^* = 38 \text{ A}$ between $2.5 \text{ s} \leq t \leq 14 \text{ s}$ (the amount of reactive power depends on grid consumption, therefore choosing $i_{dr}^* = 38 \text{ A}$ is just assumption in this example). The generator is run in the speed control mode with speed references of $\omega_{rB} = 194.3 \text{ rad/s}$ and $\omega_{rA} = 198.2 \text{ rad/s}$ which corresponds to the maximum torque T_{mB} and T_{mA} .

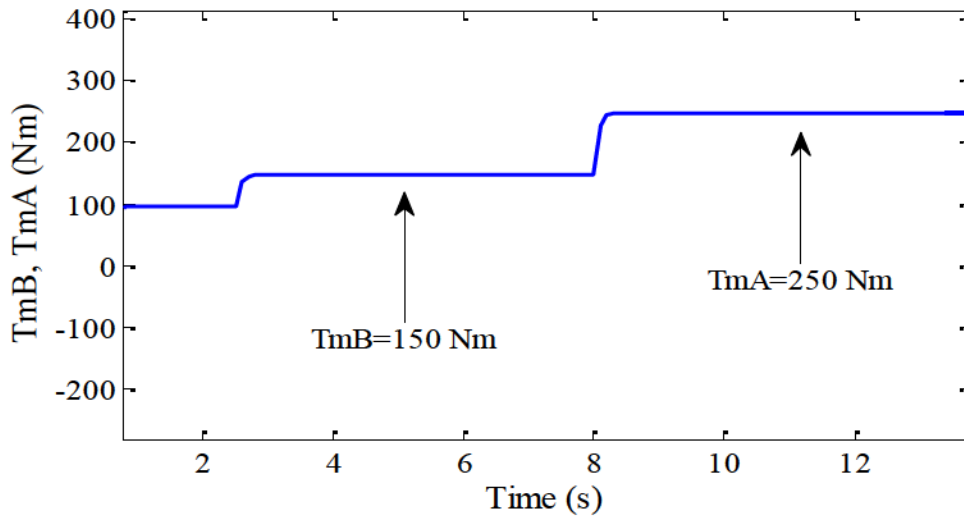


Fig. 3-7. Maximum mechanical torque

The reference for the q-axis rotor current i_{qr}^* which is the torque producing component of the rotor current is calculated according to (3.39). Through the MPPT signal from the PI controller the reference of the q-axis current is provided to extract maximum power from the wind turbine. As shown in Fig. 3-8(a), the q-axis rotor current properly follows the i_{qr}^* and Fig. 3-8(b) is a plot of

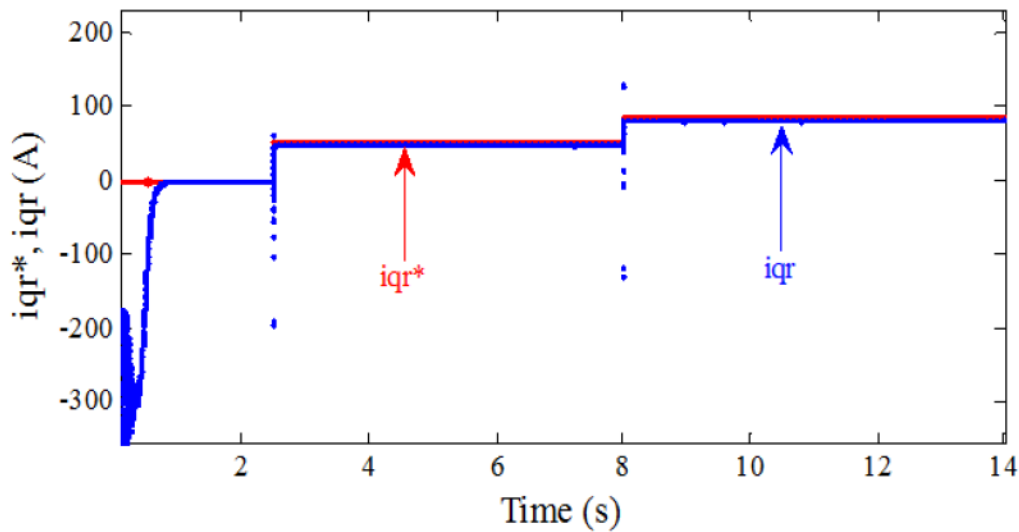


Fig. 3-8(a). q-axis rotor current

The error between the q-axis rotor current and its reference.

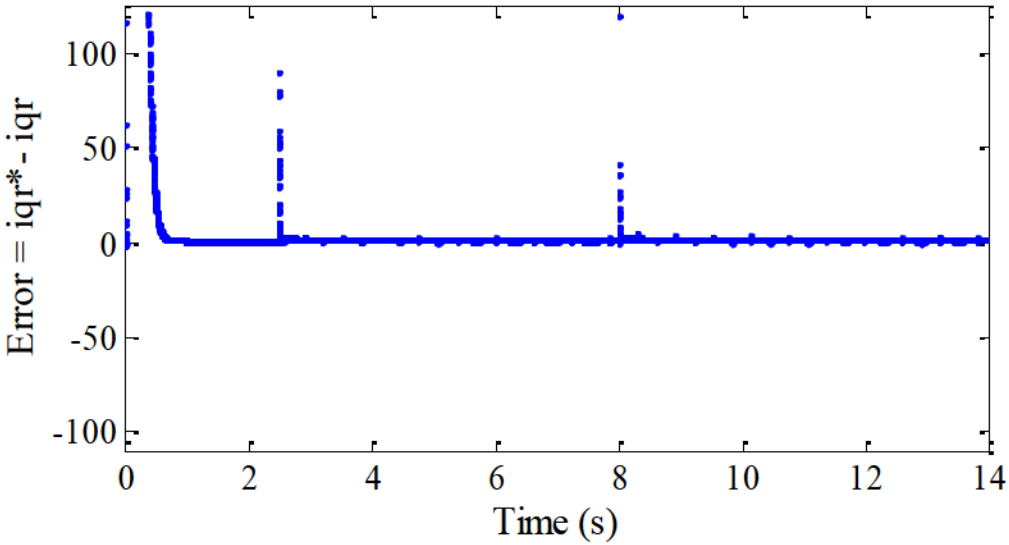


Fig. 3-8(b). Error of q-axis rotor current

After providing i_{qr}^* from MPPT algorithm, the rotor side converter responds to produce the proper v_{qr} to control DFIG rotor speed. Fig. 3-9 shows the q-axis of rotor voltage v_{qr} for different i_{qr}^* currents.

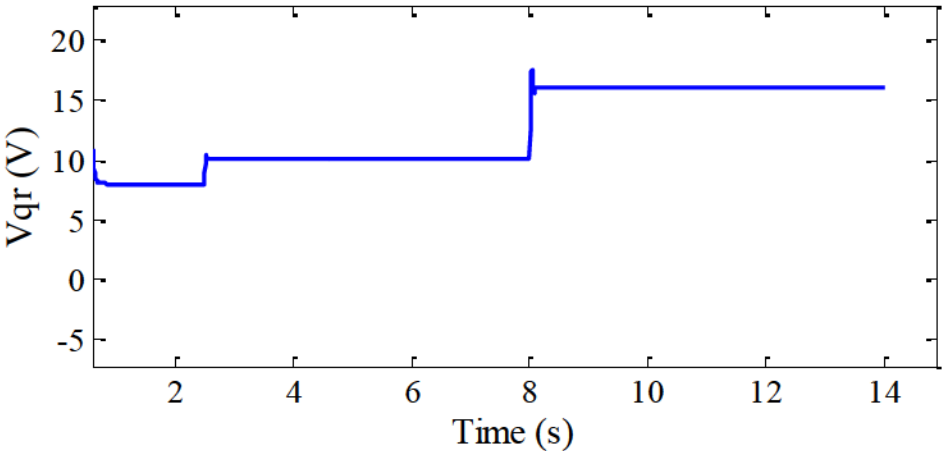


Fig. 3-9. q-axis rotor voltage

By injecting proper v_{qr} in rotor circuit from rotor side converter, the rotor speed can be regulated in order to extract the maximum power as shown in Fig. 3-10.

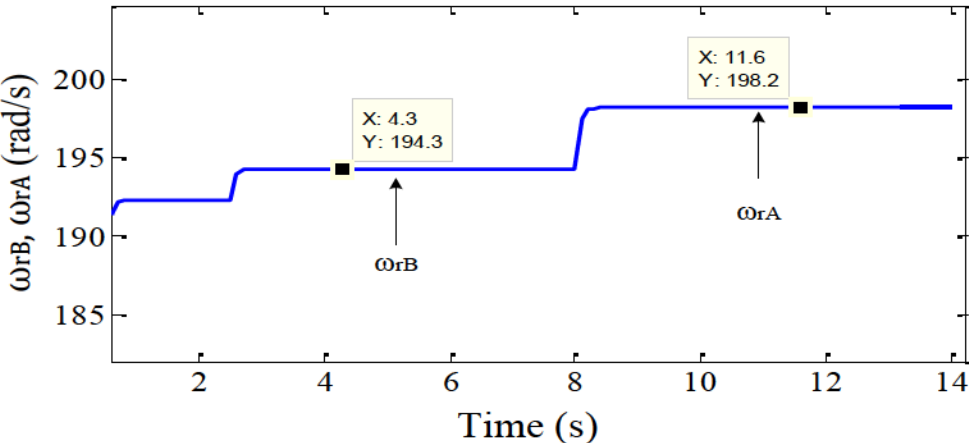


Fig. 3-10. Rotor speed corresponded to maximum torque

Fig. 3-11 shows the d-axis of rotor voltage v_{dr} for different input mechanical torque.

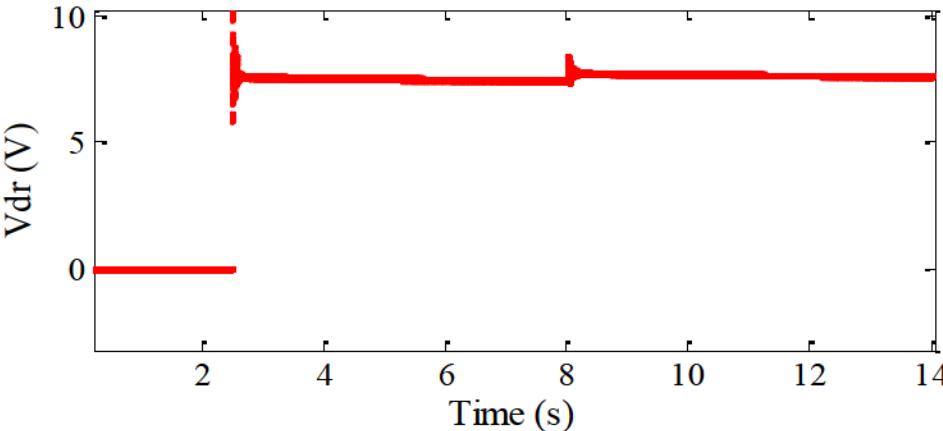


Fig. 3-11. d-axis rotor voltage

Fig. 3-12 (a) shows the d-axis of rotor current i_{dr} properly follows the i_{dr}^* to control stator reactive power and Fig. 3-12(b) shows the error of d-axis rotor current compared to its references.

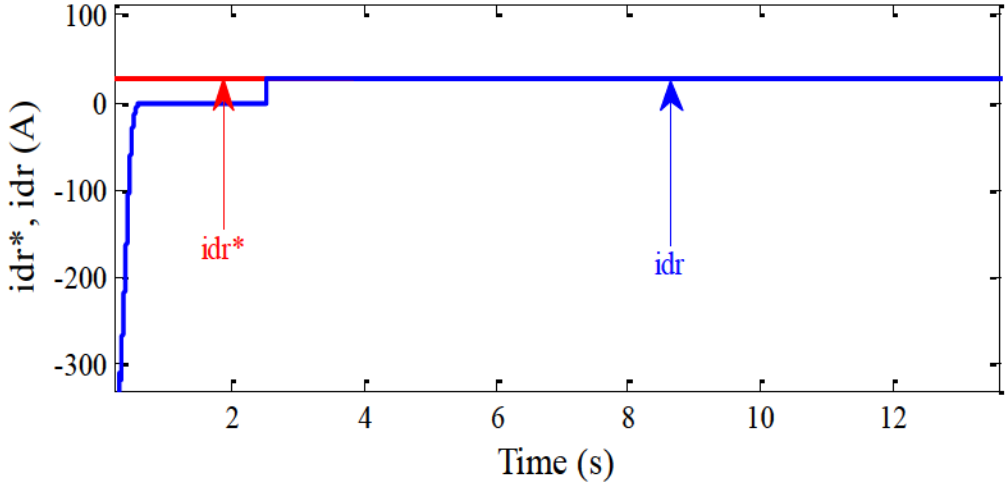


Fig. 3-12 (a). d-axis rotor current

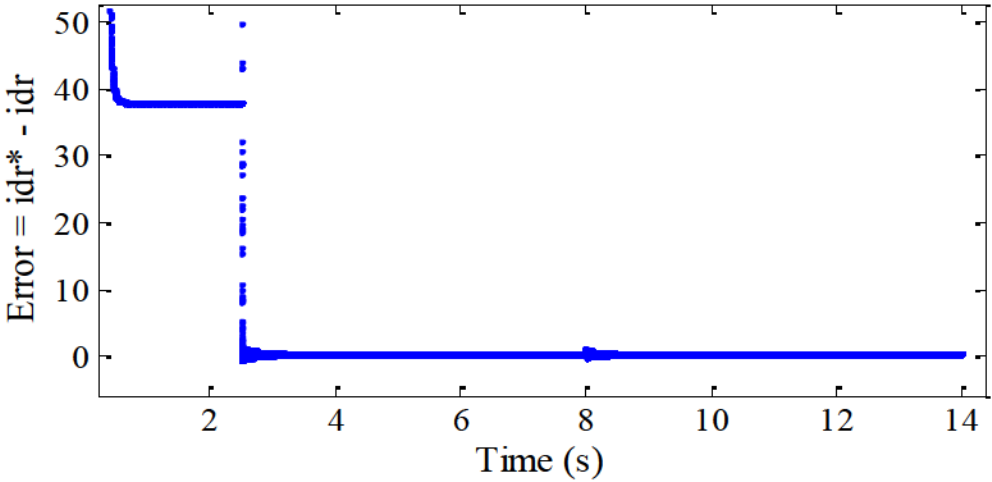


Fig. 3-12 (b). d-axis rotor current error

Fig. 3-13 shows the stator active and reactive power for different wind speed. The reactive power is controlled according to the reference of d-axis rotor current, and it is constant for different input mechanical torque.

The stator active power is derived based on maximum power point tracking and the output of active power increases due to increase in input mechanical torque and wind speed respectively.

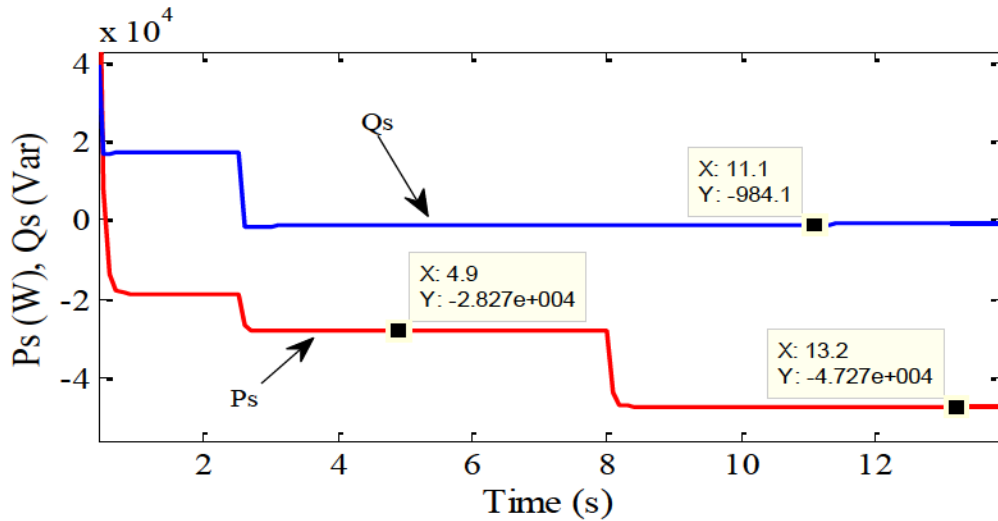


Fig. 3-13. Stator active and reactive power

The previous simulation results present the performance of the DFIG base on wind energy conversion system in steady-state. The stator flux-oriented vector control was applied to the system in order to control stator active and reactive power. To better understand power flows in the system a power balance in the steady state for this simulation is carried in the next sub-section.

3.6.2 Power balance calculations for DFIG WECS Simulation in Steady-State

The operation of the system simulated in 3.6.1 is investigated in this Sub-section at point A Fig. 3-7. The torque at point A indicates that the machine operates in super synchronous at $T_{mA} = 250$ Nm with a corresponding rotor speed of $\omega_{rA} = 198.4$ rad/s.

Fig. 3-14 shows that with DFIG operating in super synchronous mode and, the mechanical power P_m from the shaft is delivered to the grid through both stator and rotor circuits. The rotor power P_r is transferred to the grid by power converters in the rotor circuit, and the stator active power P_s is delivered to the grid directly. Neglecting the losses in the generator and converters, the power delivered to the grid P_g is the same as mechanical power P_m of the generator.

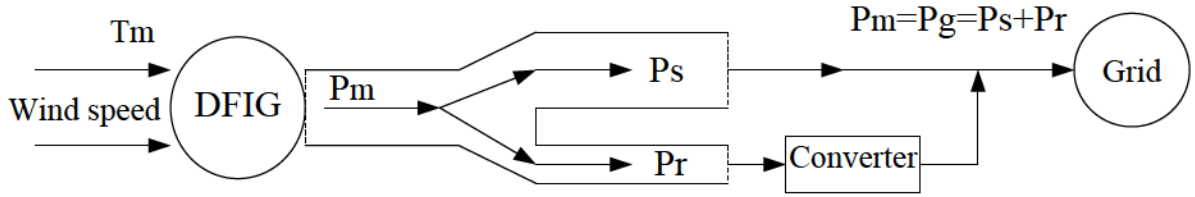


Fig. 3-14 Power flow in DFIG wind energy conversion system

The rotor power, input power and grid power can be expressed by

$$P_r = T_m * \omega_{slip} \quad (3.54)$$

$$P_m = T_m * \omega_r \quad (3.55)$$

$$P_g = P_s + P_r \quad (3.56)$$

For $T_{mA} = 250$ Nm and rotor speed $\omega_{rA} = 198.2$ rad/s, the slip frequency can be calculated as:

$$\omega_{slip} = (2/P) \omega - \omega_r \quad (3.57)$$

Where $\omega = (2\pi 60)$ is stator angular frequency, and synchronous speed is $\omega_s = (2/P) \cdot \omega$

According to the Fig. 3-10, the rotor speed at point A is $\omega_{rA} = 198.2$ rad/s, thus:

$$\omega_{slip} = -9.8 \text{ rad/s.}$$

The input mechanical power P_m and the rotor power P_r can be obtained from (3.54) and (3.55)

$$P_{mA} = 250 * (198.2) = 49.55 \text{ kW} \quad (3.58)$$

$$P_r = 250 * (-9.1) = -2.27 \text{ kW} \quad (3.59)$$

And the stator active power can be derived from Fig. 3-13 which is equal to $P_s = -47.27$ kW

The grid side active power is sum of the stator active power and rotor active power that transferred to the grid from stator and rotor side of the DFIG respectively.

$$P_g = P_s + P_r \quad (3.60)$$

$$P_g = -47.27 - 2.27 = -49.54 \text{ kW} \quad (3.61)$$

By neglecting losses in the generator and converter, the input mechanical power P_m is the same as power in the grid P_g . The negative sign in P_s and P_r indicate that the power is delivered to the grid when the system operates in super synchronous mode.

Chapter 4

Modified New Speed Control Scheme for Wound Rotor Induction Machine

A strategy that does not use rotor quadrature current reference but instead generate v_{qr} from measured i_{qr} and negative slip in wound rotor induction machine for stator flux vector control is studied by simulations in this chapter. The advantage of this approach is that it seeks to eliminate the MPPT sensor.

The magnitude of the combination of $(-\omega_{slip})$ and $L_r i_{qr}$ produces a positive voltage in generator mode which is able to decrease the rotor speed from super synchronous toward synchronous speed, and also the combination of ω_{slip} and $L_r i_{qr}$ produces a negative voltage in motor mode which is able to increase the rotor speed from sub synchronous to synchronous speed.

In (4.1) and (4.2) the v_{qr} is expressed in generator and motor- mode for wound rotor induction machine respectively in the new scheme control strategy.

$$v_{qr} = (-\omega_{slip} L_r i_{qr}) \quad (4.1)$$

$$v_{qr} = (\omega_{slip} L_r i_{qr}) \quad (4.2)$$

The rotor inductance L_r can be considered as constant and its numerical value used in the simulations is obtained from Table. 3-1 as:

$$L_r = L_{lr} + L_m = \frac{X_{lr}}{\omega} + \frac{X_{lm}}{\omega} = 0.035 \quad (4.3)$$

(4.1) and (4.2) only synchronize the rotor speed in both operation of induction machine, therefore it is possible to regulate the rotor speed in wide range by controlling the value of $\omega_{slip} L_r i_{qr}$. (4.4) and (4.5) show the ability to control rotor speed for wound rotor induction machine by adjusting a constant k.

$$v_{qr} = k(0.035) * (-\omega_{slip} i_{qr}) \quad (4.4)$$

$$v_{qr} = k(0.035) * (\omega_{slip} i_{qr}) \quad (4.5)$$

The constant k has been obtained by simulations for the machine with parameters in Table. 3-1 and the range of values are shown graphically in Fig. 4-1 and the maximum value of k is shown in Table 4-1 for specific torque levels. The maximum values are further discussed.

Fig. 4-1 illustrates the speed control of wound rotor induction machine when the operating point is either in generator mode or in motor mode for the new control scheme.

The following two examples illustrate the use of the Table. 4-1 and Fig. 4-1 in selecting k for a given situation:

Example 1. Assume the machine initially operates in the generator mode with an input mechanical torque $T_m = 250$ Nm with a rated rotor speed of ω_{rA} as indicated by point A in Fig. 4-1. If the controller decides to increase the rotor speed from point A to maximum rotor speed which is selected as 20% of synchronous speed in this thesis, the k is changed from zero to $k_{max} = -0.25$ where the range of k_{max} is indicated in Table 4-1, and the size of k_{max} depends on input mechanical torque, maximum rated speed and machine's size. Also if the controller decides to decrease the rotor speed from point A to synchronous speed, the k is changed from zero to one and gradually rotor speed will be established around synchronous speed at $\omega_r \cong \omega_s$.

Example 2. Assume the wound rotor induction machine operates in motor mode as indicated by point B in Fig. 4-1. In this case the mechanical input torque is $T_m = 150$ Nm with a rated rotor speed of ω_{rB} . If the controller decides to increase the rotor speed from point B to synchronous speed, the k will be changed from zero to one, and gradually rotor speed will be established around synchronous speed $\omega_r \cong \omega_s$.

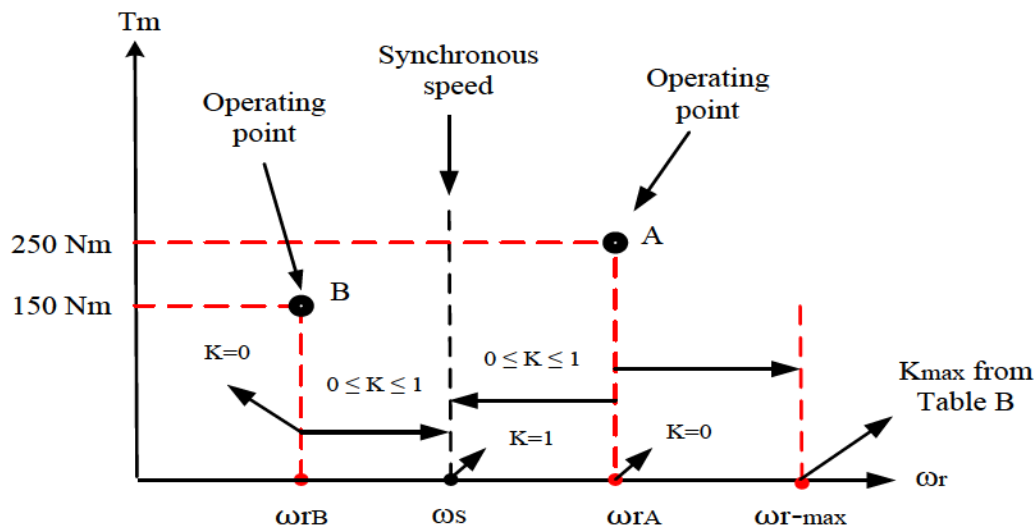


Fig. 4-1. Variation of k for different operating point

| T _m N.m | 50 Nm | 100 Nm | 150 Nm | 200 Nm | 250 Nm |
|--------------------|-------|--------|--------|--------|--------|
| K _{max} | -1.8 | -0.8 | -0.5 | -0.35 | -0.25 |

Table. 4-1: k_{\max} for 50 hp Induction Machine with $\omega_{r-\max} = 1.2 \omega_s$

4.1 Simulation result for New Speed Control Scheme

The simulation results of this Section illustrate the accuracy of the control scheme for two type of machine's operation (generator and motor-mode).

Fig. 4-2 shows the control of rotor speed in generator mode that was expressed in Example 1. Machine initially operates in generator mode as indicated in point A in Fig. 4-1. The point A is presented in Fig. 4-2 with an input mechanical torque $T_{mA} = 250$ Nm and rated rotor speed $\omega_{rA} = 198.2$ rad/s.

As shown in Fig. 4-2, in order to increase the rotor speed from operating point $\omega_{rA} = 198.2$ rad/s to maximum rotor speed $\omega_{r-\max} = 223.9$ rad/s, the magnitude of k should be decreased from zero to $k_{\max} = -0.25$, and for decreasing the rotor speed from $\omega_{r-\max}$ to close to synchronous speed $\omega_r \cong \omega_s \cong 190.9$ rad/s, the magnitude of k should be increased from k_{\max} to one. Fig. 4-2 shows the proper performance of the new speed control in generator mode for induction machine.

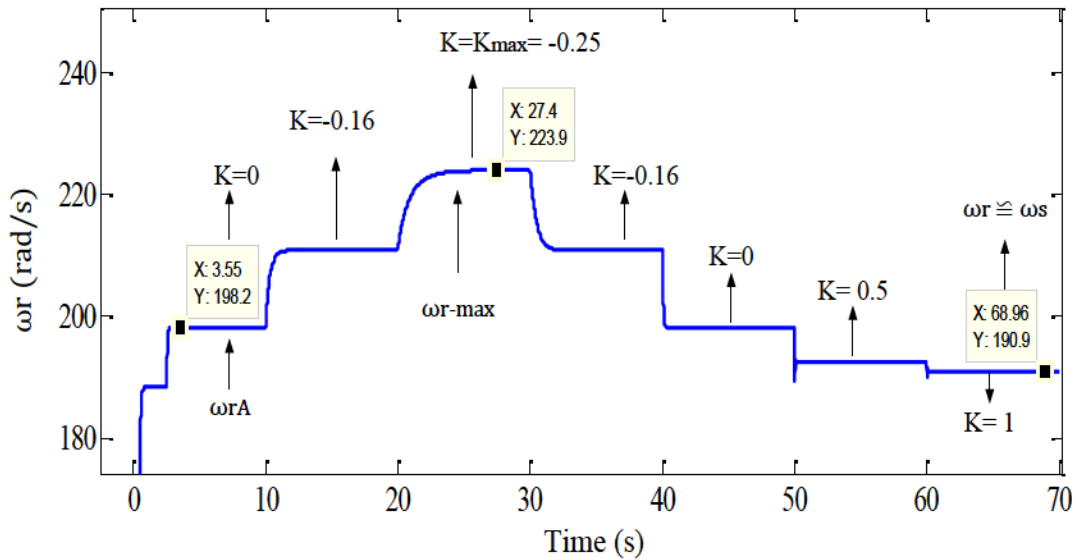


Fig. 4-2. Control rotor speed in generator mode (X is Time and Y is ω_r)

Fig. 4-3 shows the control of rotor speed in motor mode for the operating point expressed in Example 2 in the previous Section. Machine initially operates in motor mode as indicated in point B in Fig. 4-1. The point B is presented in Fig. 4-3 with an input mechanical torque $T_{mB} = 150$ Nm and rated rotor speed $\omega_{rB} = 184.3$ rad/s.

In order to increase the rotor speed from operating point $\omega_{rB} = 184.3$ rad/s to close to synchronous speed $\omega_r \cong \omega_s \cong 187.3$ rad/s, the magnitude of k should be increased from zero to one. Fig. 4-3 shows the proper performance of a new speed control in motor mode for induction machine.

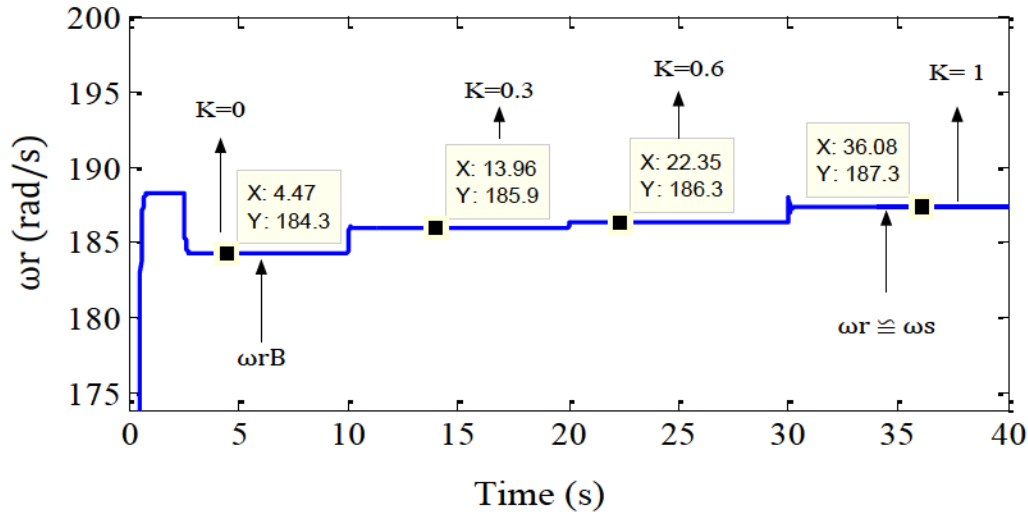


Fig. 4-3. Control rotor speed in motor mode (X is Time and Y is ω_r)

This new scheme simplified and improved the speed control for wound rotor induction machine over conventional PI controller, with no extra current control loops being required. The impact of machine parameter variations on system performance is negligible (no effect of machine inductance or resistance is in new equation of v_{qr}).

4.2 Sensorless Maximum Power Point Tracking with New Speed Control Scheme for DFIG

It can be observed from Fig. 4-4 that the maximum of the power curve, for particular wind speed (v_w), occurs at a particular rotor speed. Due to the aerodynamic characteristics of a wind turbine, a small variation from the optimum rotor speed will cause a significant decrease in the power extracted from the wind. Turbines do not naturally operate at the optimum wind speed for any given wind velocity because its rotor speed depends on the generator loading as well as the wind speed fluctuations. Because of this, non-optimized conversion strategies lead to a large percentage of wasted wind power [11, 21].

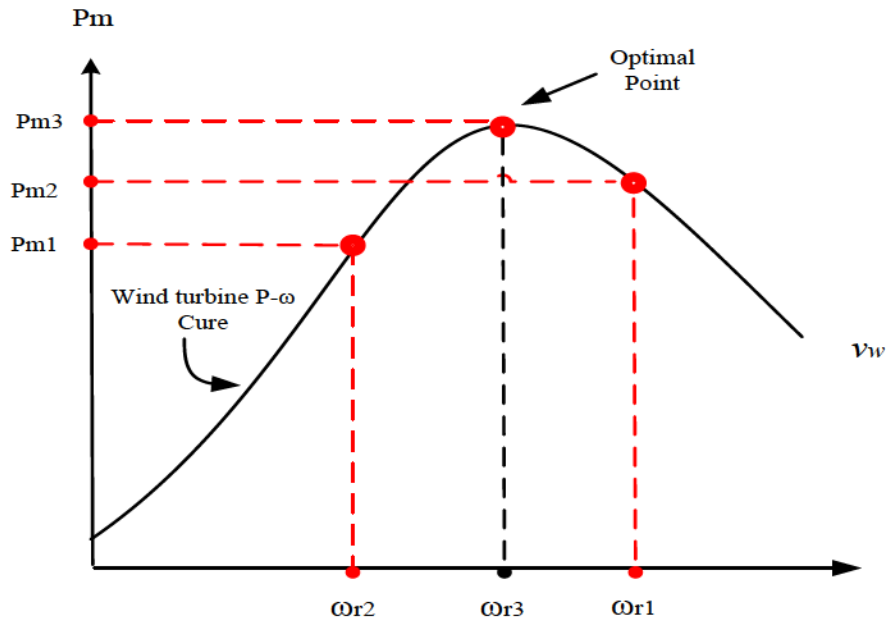


Fig. 4-4. Power curve versus rotor speed

The purpose of this section is to control the rotor speed of the DFIG toward extracting maximum power from the wind turbine with the help of a new speed control scheme and hill climb searching (HCS) algorithm [22].

4.2.1 Modified Hill Climb Search

As indicated in [22, 23], the Hill Climb Search (HCS) control happens to be the one that does not require any prior knowledge of the system and is absolutely independent of the turbine, generator, and wind characteristics. Therefore, the HCS control bears the potential to be the most appropriate choice for MPPT. The maximum power point is defined by the power curve in Fig. 4-5 where $\Delta P = 0$. The purpose of the HCS is to climb the curve by changing the rotor speed and measuring the output power until the condition of $\Delta P = 0$ is achieved.

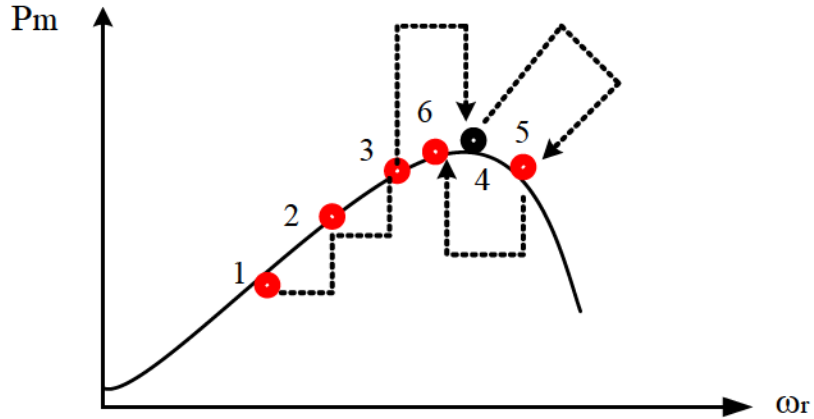


Fig. 4-5. Power versus rotor speed

The system starts at point 1 and decided to move to point 2 by increasing the rotor speed. It shows that by increasing in the rotor speed the magnitude of power will be increased positively therefore the control system will increase the rotor speed to point 3. Since ΔP is positive, the system is climbing up the power curve to the next point. If ΔP still positive, the control system will send signals to increase the rotor speed to point 5.

In point 5 the ΔP is negative due to increase in speed and at this point the optimum point has been passed. Therefore the rotor speed is decreased to point 6.

The control system will oscillate and will settle at the point that $\Delta P = 0$ where is called maximum power point. The HCS concept is described in detail based on applying the new scheme to control rotor speed in Section 4.2.2 with simulations.

4.2.2 MPPT Control with the HCS Algorithm and a new Speed Control Scheme for the DFIG with Simulation Results.

Assume the DFIG operates in super synchronous mode and in steady-state condition with an operating point A and optimal point C, that input mechanical torque and corresponding rotor speed in optimal point C are $T_{mc} = 150 \text{ Nm}$ and $\omega_{rc} = 195.1 \text{ rad/s}$. The knowledge of location of operating point is unknown. In order to determine the location of operating point in power curve, there are two possibilities, whether the current operating point is to the right of the optimal point or to the left of the optimal point on the power curve.

As shown in Fig. 4-6, decreasing in rotor speed causes the point A to move to the point B, therefore P_B is less than P_A , thus, $\Delta P = P_B - P_A < 0$ that means operating point is to the left side of the optimal point, otherwise it is on the right side of the optimal point which is indicated in Fig. 4-7 where $\Delta P = P_B - P_A > 0$.

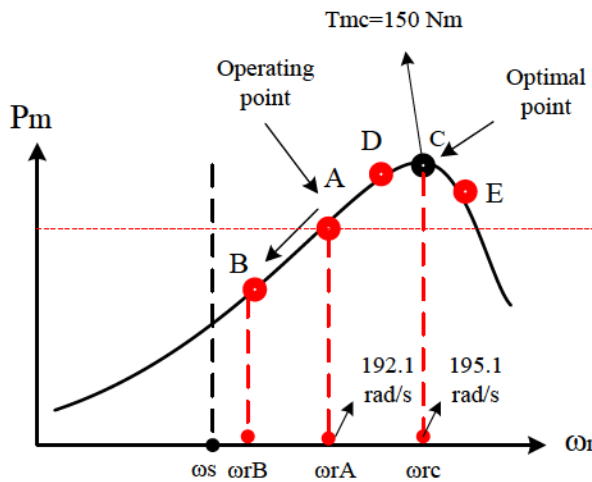


Fig. 4-6. Power versus rotor speed

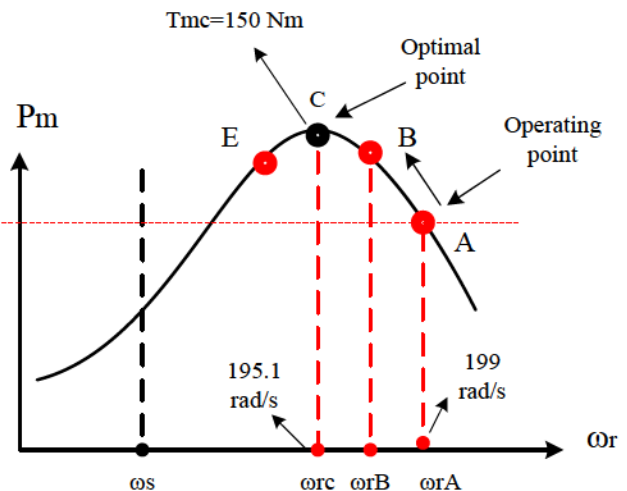


Fig. 4-7. Power versus rotor speed

For the simulations shown in Fig. 4-8, for case one, assume the operating point A is on the left side of the optimal point C as in Fig. 4-6, where the input mechanical torque in point A is $T_{mA} = 100 \text{ Nm}$ and rotor speed is $\omega_{rA} = 192.1 \text{ rad/s}$. In order to achieve the optimal point in this case, the controller send signals to increase the rotor speed toward the optimal point C.

Therefore to control rotor speed with the new scheme strategy, (4.4) is used to regulate the rotor speed (because the machine operates in super synchronous mode), and to increase the rotor speed from point A to point C in Fig. 4-6, the k will be changed from zero to k_{max} where the k_{max} is equal to -0.8 as indicated in Table 4-1.

The simulation result in Fig. 4-8 which is connected to Fig. 4-6 shows the rotor speed increased gradually from operating point A to point D, since $\frac{\Delta P}{\Delta \omega}$ positive, the system is climbing up the power curve. If $\frac{\Delta P}{\Delta \omega}$ still positive, the system continues to increase the rotor speed to point E.

The algorithm notices that the change in power from point D and point E is negative, and it was due to increase in speed. If $\frac{\Delta P}{\Delta \omega}$ now negative, the optimum point has been passed. As a result, the rotor speed is decreased to point C and optimum power point is achieved.

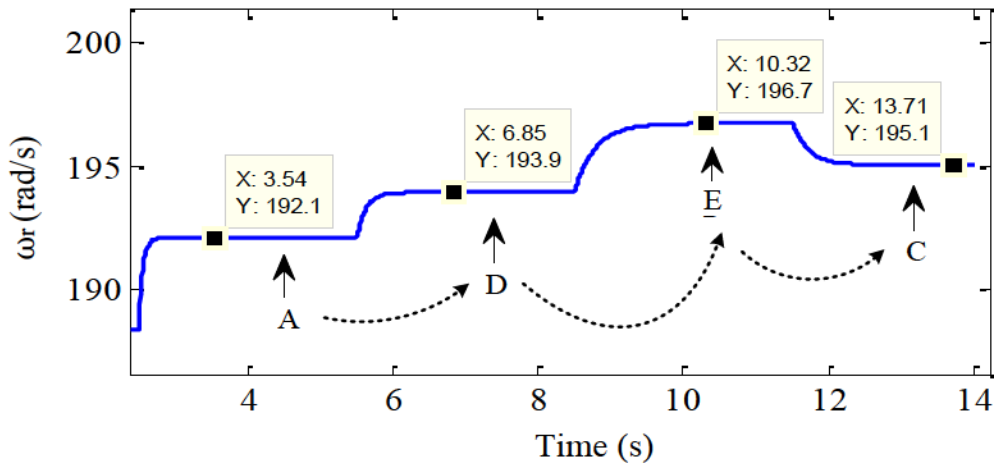


Fig. 4-8. MPPT with rotor speed regulation

For the simulations shown in Fig. 4-9, for case two, assume the operating point A is on the right side of the optimal point C as in Fig. 4-7, where the input mechanical torque in point A is $T_{mA} = 100$ Nm and rotor speed is $\omega_{rA} = 199$ rad/s. As in case one (4.4) is used, but magnitude of k will be changed from zero toward one in this case. Therefore the rotor speed decreases from operating point A to optimal point C.

The simulation result in Fig. 4-9 which is connected to Fig. 4-7, shows the rotor speed decreased gradually from operating point A to point B, since $\frac{\Delta P}{\Delta \omega}$ positive, the system is climbing up the power curve. If $\frac{\Delta P}{\Delta \omega}$ still positive, the system continues to decrease the rotor speed to point E. The algorithm notices that the change in power from point B to point E is negative, and it was due to decrease in speed. Since if $\frac{\Delta P}{\Delta \omega}$ now negative, the optimum point has been passed. As a result, the rotor speed is increased to point C.

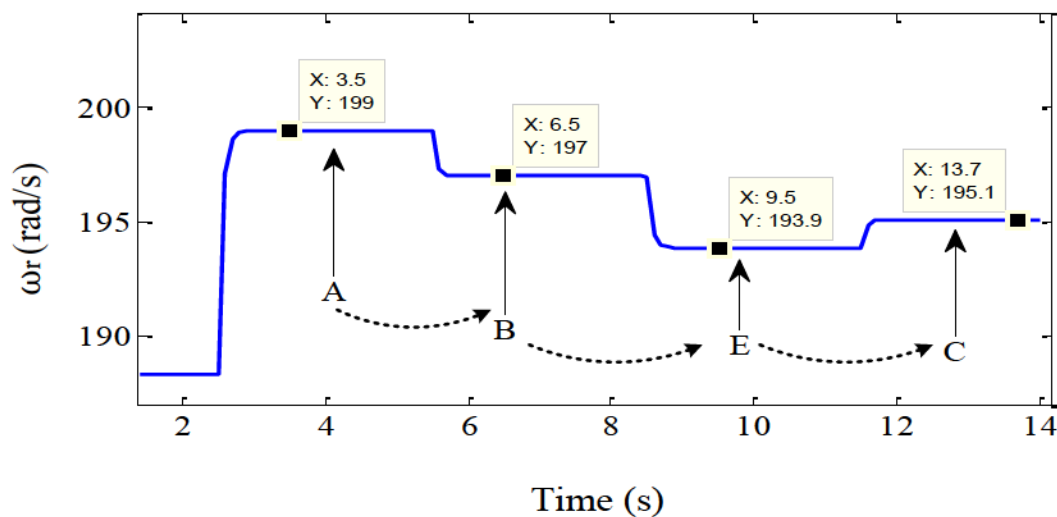


Fig. 4-9. MPPT with rotor speed regulation

In Chapter 2, the maximum power point tracking (MPPT) control with sensor was introduced for DFIG wind energy conversion system. The major disadvantage of this scheme of control, is that the knowledge of the wind speed is required which is measured by a wind speed sensor, these mechanical sensor increase the cost (equipment and maintenance cost) and reduce the reliability of the overall wind turbine generator system [24]. In order to eliminate the use of MPPT sensor and complexity of estimation of the reference i_{qr}^* , the control of DFIG with sensorless maximum power point tracking has been investigated in Section 4.2 with the help of a new simplified speed control strategy in this chapter. Simulation results obtained in this Chapter verify the proper operation of the system in this new speed control scheme and that MPPT can be performed with this new control scheme, in a sensorless way, by using hill climbing techniques.

Chapter 5

A New Rotor Position-Sensorless Scheme for Doubly Fed Induction Generator

The rotor position is obtained by a position encoder and the stator flux angle is obtained by hardware or software phase lock loop (PLL). The criticality of the angle measurements has been made clear from insulated gate bipolar transistor (IGBT) failures in factory tests on a prototype 1500 kW DFIG [25]. Following the failure, the vector controlled DFIG was monitored closely, and in a 4hr period, it was found that the incremental encoder picked up extraneous noise four times in the reset pulse. The wrong angular measurements mean that the d-q reference frames of the stator and the rotor will become misaligned. This leads to: 1) the DFIG perceiving wrong active and reactive power reference settings, resulting in very large steady-state destructive currents and 2) system instability also lead to large destructive currents [25].

There are several approaches for the control of DFIG in all the methods implemented, the performance of the system depends on the knowledge of the mechanical position of the rotor, derived from a position encoder, or from position-sensorless estimation algorithm as consider in this chapter [26, 27].

There are major challenges in design of position-sensorless estimation scheme for DFIG. The algorithm should be stable and work well at any speed in the working range including near synchronous speed. The rotor position-sensorless estimation should be able to start on the fly, that is, it should converge to the correct position after some period of time, when the system starts working without the knowledge of initial conditions [26].

A new position-sensorless method and its stability study for the estimation of slip angular frequency (ω_{sl}) for the wound-rotor induction machine is presented in this chapter. The main purpose of this study is to implement the control of the doubly fed induction generator. This method does not need any information about initial rotor position and it is not dependent on machine's parameters, it is based on measurement of $i_{abc r}$ and analysis of behavior of $i_{\alpha\beta r}$ in the d-q axis synchronous reference frame or in any x-y axis arbitrary reference frame after transformation.

In [14], it is shown that the behavior of variables such as (rotor and stator current and voltage) in synchronous reference frame are constant in steady-state, while in an arbitrary reference frame they vary with time. By this principle, one is able to estimate the slip angular frequency (ω_{slip}) to transfer rotor variables to d-q axis synchronous reference frame. The proposed sensorless algorithm is explained with the help of Figs. 5-1 and 5-2.

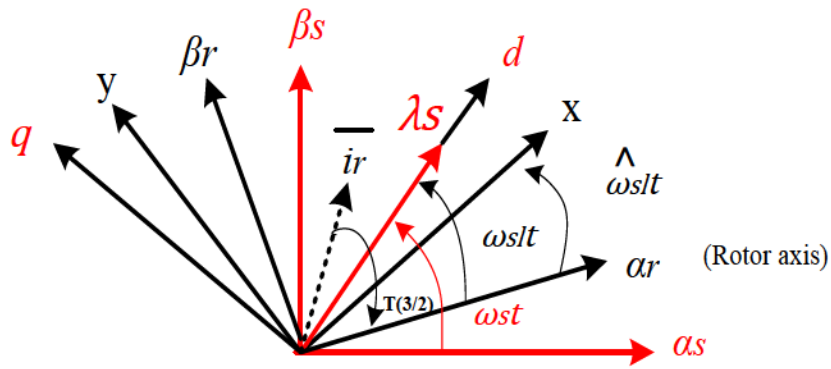


Fig. 5-1 Space vector diagram to transfer i_{abc-r} to $i_{\alpha\beta r}$ and then to i_{dq}

The rotor current in $\alpha\beta_r$ stationary (frame fixed to the rotor) reference frame will be divided in $i_{\alpha r}$ and $i_{\beta r}$ and these two current should be transferred to d-q axis synchronous reference frame to obtain a stator flux oriented vector control. In order to achieve stator flux vector control, the correct estimation of ω_{sl} is required to make $\alpha\beta_r$ vectors current exactly aligned with d-q axis frame after transformation.

As shown in Fig. 5-2, the result of a mistake in estimation in the ω_{sl} which is called $\hat{\omega}_{sl}$ causes the $i_{\alpha r}$ and $i_{\beta r}$ to be transferred to an arbitrary x-y axis reference frame where they will vary with time and $i_{\alpha r}$ and $i_{\beta r}$ are not constant in the steady-state in the arbitrary x-y axis reference frame after transformation.

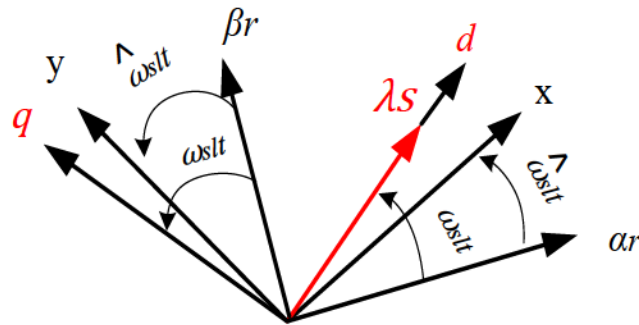


Fig. 5-2. Space vector diagram to transfer variables from $\alpha\beta r$ to d-q frame or x-y frame

Fig. 5-3 and Fig. 5-4 will illustrate the above idea for an input mechanical torque of $T_m = 150$ Nm applied to the DFIG considered in Chapter 3. The result of transformation of i_{ar} is aligned with d-axis frame and constant due to correct estimation of ω_{sl} in the interval $2.5 \text{ s} \leq t \leq 15 \text{ s}$, but the result of transformation of i_{ar} is aligned with an arbitrary x-axis frame and fluctuates in this frame due to incorrect estimation of ω_{sl} in the interval $15 \text{ s} \leq t \leq 65 \text{ s}$.

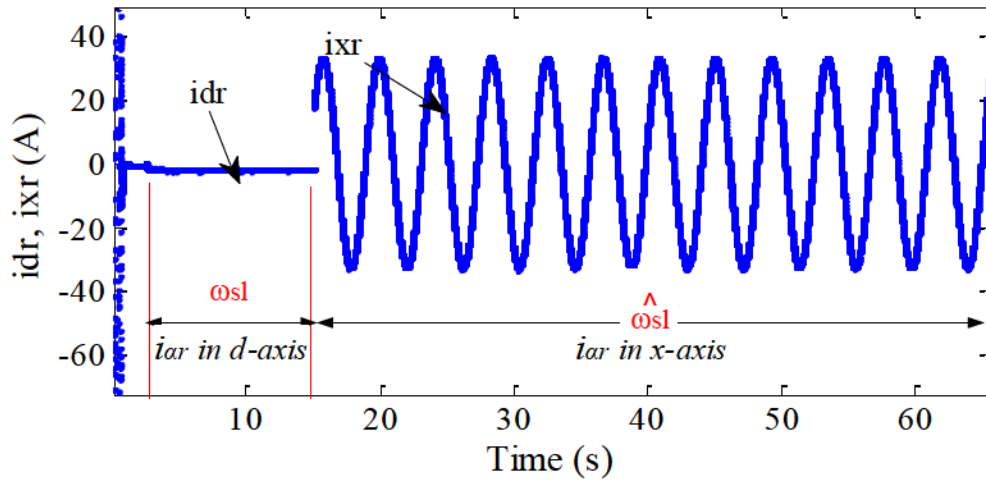


Fig. 5-3. i_{ar} in d-axis (synchronous frame) and in x-axis (arbitrary frame) when error is 1.5 rad/s

In Fig. 5-3, the i_{xr} fluctuates at high frequency due to the big error of slip angular velocity estimation which is equal to 1.5 rad/s. In Fig. 5-4 the i_{xr} fluctuates at low frequency due to low error in slip angular frequency estimation which is equal to 0.087 rad/s, when the error approaches to zero the i_{xr} will be matched with i_{dr} and $\hat{\omega}_{sl}$ will be equal to ω_{sl} respectively.

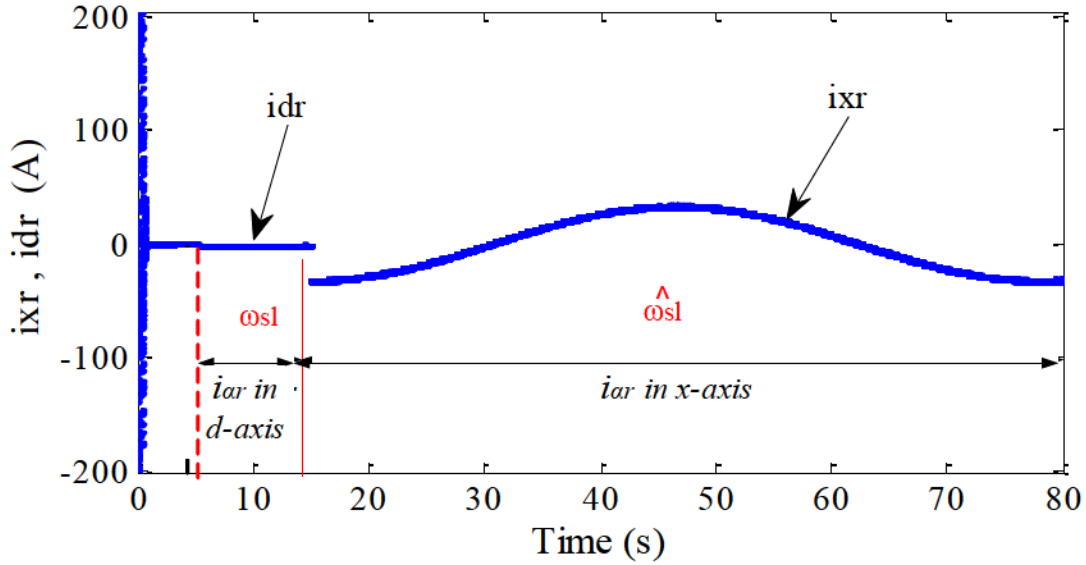


Fig. 5-4. i_{ar} in d-axis (synchronous frame) and in x-axis (arbitrary frame) when the error is 0.087 rad/s

5.1 Preliminary Computation

In [28], it is assumed that the wound rotor machine current can be measured directly and the rotor currents are function of $\omega_{slip}(t)$ for balanced direct system and can be expressed by

$$i_{abcr}(t) = \begin{cases} I_m \cos(\omega_{slip} t) \\ I_m \cos(\omega_{slip} t - \frac{2\pi}{3}) \\ I_m \cos(\omega_{slip} t + \frac{2\pi}{3}) \end{cases} \quad (5.1)$$

A 3/2 Concordia's transformation allows to define current i_{ar} and $i_{\beta r}$ [28].

$$\begin{bmatrix} i_{ar} \\ i_{\beta r} \end{bmatrix} = T_{(3/2)} \cdot \begin{bmatrix} i_{ar} \\ i_{br} \\ i_{cr} \end{bmatrix} = \begin{cases} i_{ar} = I_m \cos \omega_{slip} t \\ i_{\beta r} = I_m \sin \omega_{slip} t \end{cases} \quad (5.2)$$

Where,

$$T_{(3/2)} = \left(\frac{3}{2}\right) \cdot \begin{bmatrix} 1 & -0.5 & -0.5 \\ 0 & \sqrt{3/2} & -\sqrt{3/2} \\ 0.5 & 0.5 & 0.5 \end{bmatrix} \quad (5.3)$$

Park's transformation leads to i_{dr} and i_{qr} :

$$\begin{bmatrix} i_{dr} \\ i_{qr} \end{bmatrix} = T_{(\omega_{sl})} \cdot \begin{bmatrix} i_{\alpha r} \\ i_{\beta r} \end{bmatrix} \quad (5.4)$$

Where,

$$T_{(\omega_{sl})} = \begin{bmatrix} \cos(\omega_{sl}^{\wedge} t) & \sin(\omega_{sl}^{\wedge} t) \\ -\sin(\omega_{sl}^{\wedge} t) & \cos(\omega_{sl}^{\wedge} t) \end{bmatrix} \quad (5.5)$$

The slip angular frequency of ω_{sl}^{\wedge} in (5.5) can be from k_1 to k_2 , where k_1 and k_2 are presented as below:

$$k_1 = -(\omega_s - \omega_{r_max}), \omega_{r_max} = 1.2 \omega_s \longrightarrow k_1 = -0.2\omega_s \quad (5.6)$$

$$k_2 = (\omega_s - \omega_r), \omega_{r_max} = 1.2 \omega_s \longrightarrow k_2 = 0.2\omega_s \quad (5.7)$$

(5.6) and (5.7) indicate that the range of slip angular frequency is determined in this thesis when the rotor speed is 20% above and below the synchronous speed (k_1 for generator-mode and k_2 for motor-mode) and only one slip angular frequency will be correct and equal to ω_{slip} which makes the i_{dr} and i_{qr} constant and aligned with d-q axis synchronous reference frame in steady-state and the other angular frequencies are incorrect. The behavior of $i_{\alpha r}$ and $i_{\beta r}$ after transformation is changed in magnitude and frequency by different estimated value of ω_{sl}^{\wedge} . The new position-sensorless method is able to identify a frame that is aligned with $i_{\alpha r}$ and $i_{\beta r}$ after transformation.

5.2 Flowchart of Slip Angular Frequency Estimation

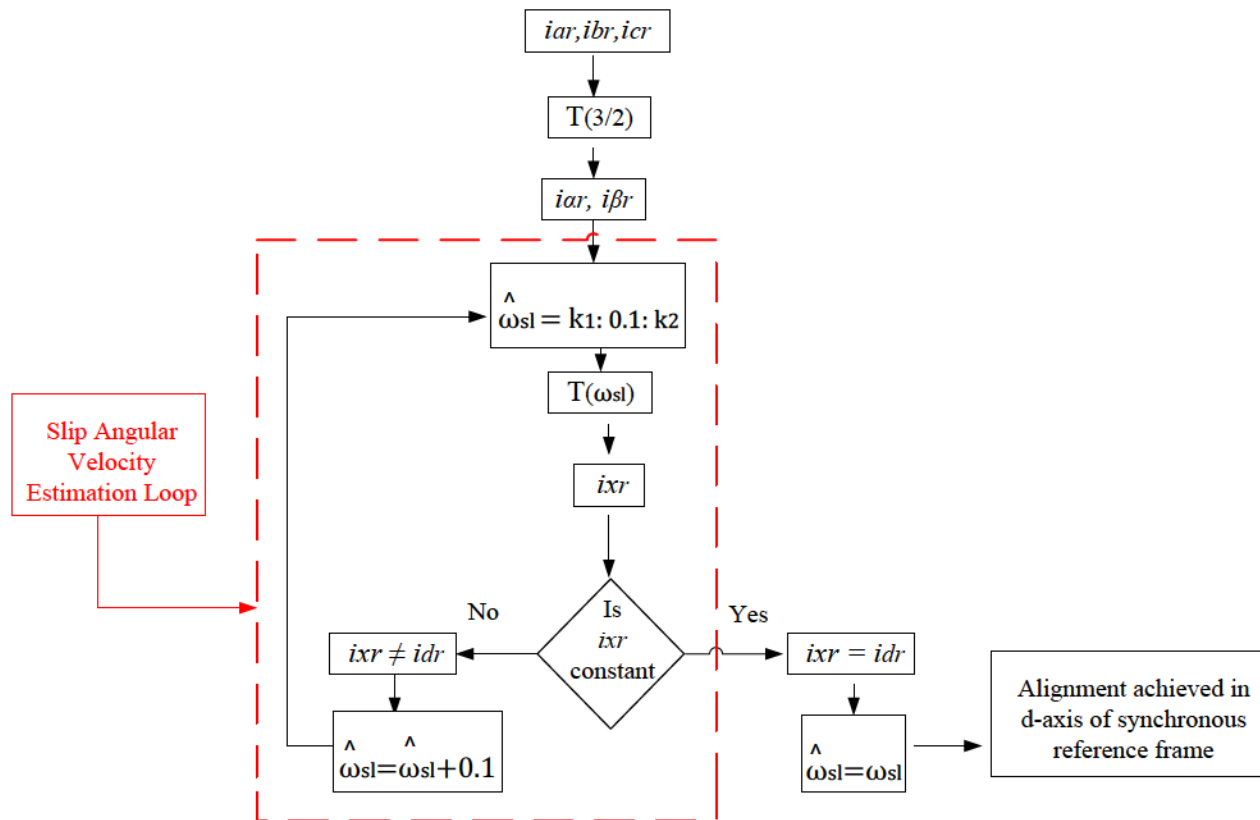


Fig. 5-5. Flowchart of slip angular frequency estimation

Fig. 5-5 shows the flowchart for slip angular frequency estimation scheme. The three phase rotor currents are directly measured as i_{ar} , i_{br} , and i_{cr} (as shown in Fig. 5-6, to get correct measurement of the three phase rotor currents we need to wait for at least 0.3 s until the system settles reasonably into the steady-state). As shown in Fig. 5-1 the vector of three phase rotor current \bar{i}_r will be transferred to the rotor stationary reference frame by (5.2) to provide i_{ar} and $i_{\beta r}$.

In order to achieve the stator flux oriented vector control, the i_{ar} and $i_{\beta r}$ have to be transferred to d-q axis synchronous reference frame to provide i_{dr} and i_{qr} which i_{dr} will be aligned with d-axis and i_{qr} with q-axis. The slip angular frequency is required to transfer rotor variables from rotor

axis to synchronous axis and vice versa. The slip angular frequency is estimated by applying different ω_{sl} in (5.4), and each ω_{sl} transfers i_{ar} to either x-axis arbitrary reference frame which is called i_{xr} or d-axis synchronous reference frame which is called i_{dr} . The new scheme is investigated in Sub-section 5.2.1 with an example. The error of angle estimation is very small (around one degree or 0017 rad/s) and the input mechanical torque for whole period of the operation is equal to 50 Nm.

5.2.1 Example

In this example it is assumed that the input mechanical torque is increased to 50 Nm at $t = 2.5$ s. As indicated in Section 5.1, the measurement of three phase rotor currents is the first step. The second step is to transfer the three phase rotor current into two phase $\alpha\beta_r$ stationary reference frame. As shown in Fig. 5-6, to get correct measurement of the three phase rotor currents we need to wait at least 0.3 s until the system settles reasonably into the steady-state.

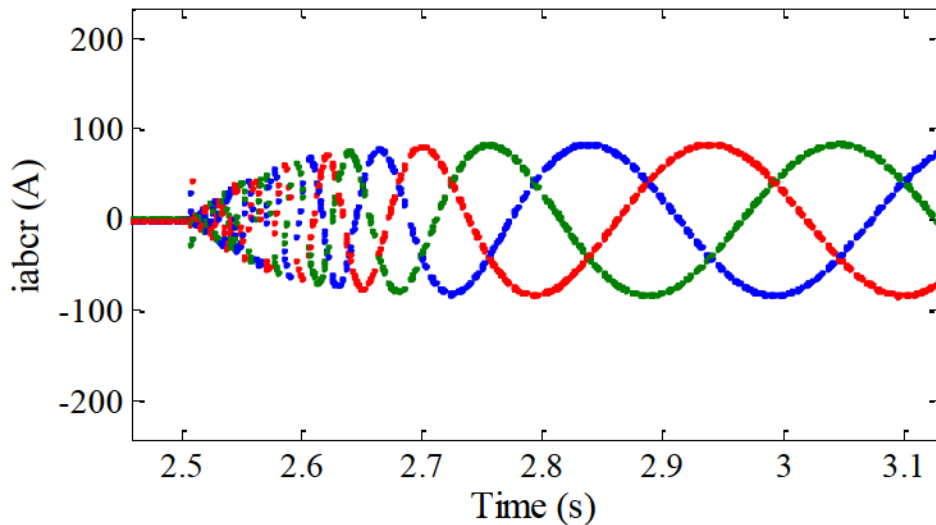


Fig. 5-6. Three phase rotor current

Fig. 5-7 illustrates the process of new position-sensorless estimation for this example. As mentioned before, after 0.3 s, the three phase rotor current are transferred into two phase $\alpha\beta_r$, then six samples of i_{ar} and $i_{\beta r}$ in the three different times will be computed. The time between two samples is 0.2 s and time for processing of slip angular frequency estimation is around 0.1 s, so the total period of estimation is 0.8 s.

It is possible to increase or decrease the sampling interval to more than or less than six samples in three different times, but less than six samples (at least four samples in two different times) decrease the accuracy of slip angular frequency estimation and more than six samples will increase the estimation time, therefore taking six samples gives reasonable accuracy in slip angular frequency estimation in short period of time.

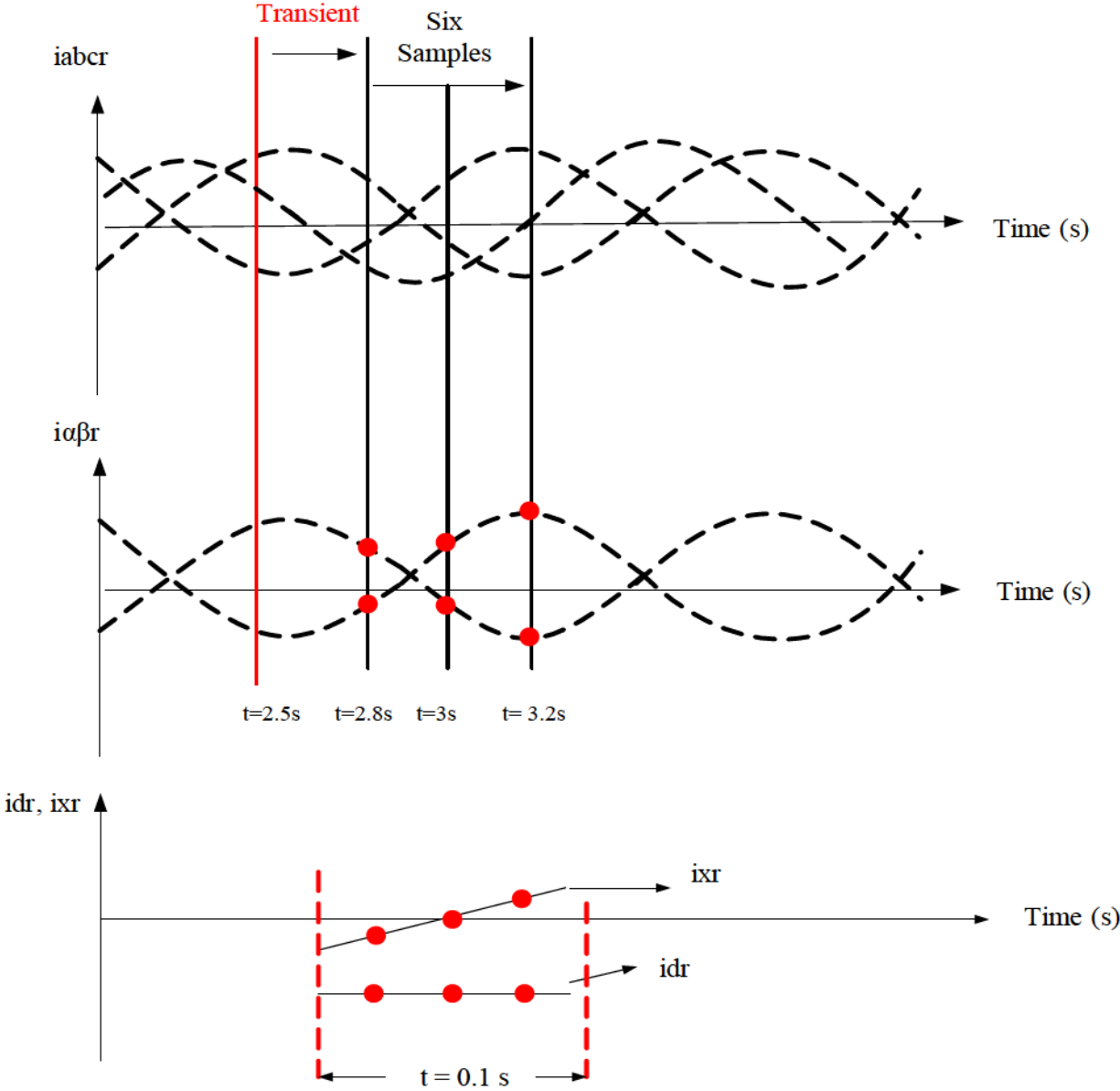


Fig. 5-7. Process of slip angular frequency estimation

Fig. 5-8, shows the behavior of i_{dr} and i_{xr} in synchronous reference frame and in arbitrary reference frame respectively. As we can see the i_{xr} is not constant after transformation due to error in estimation, but in the other hand i_{dr} is constant because of correct estimation. Fig. 5-9 shows the computation of slip angular frequency in this new scheme.

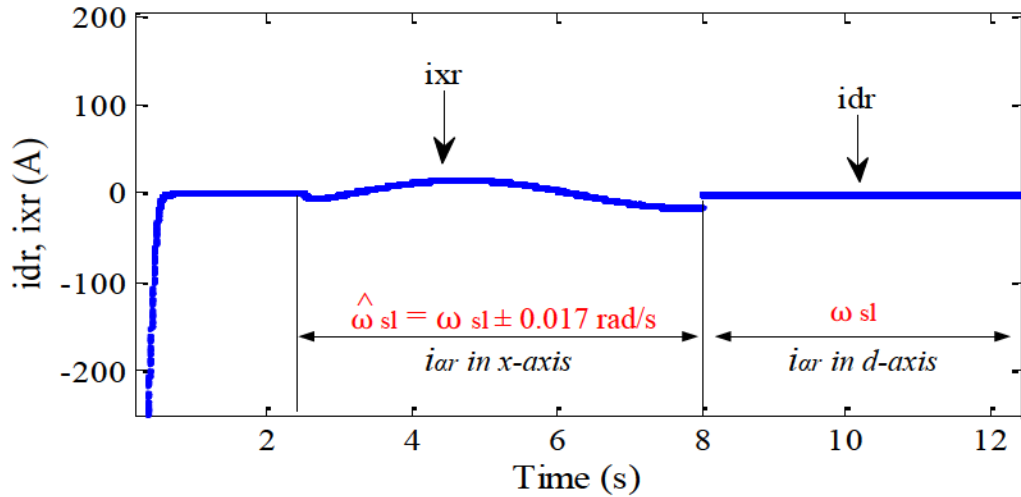


Fig. 5-8. i_{dr} and i_{xr} when the error is 0.017 rad/s

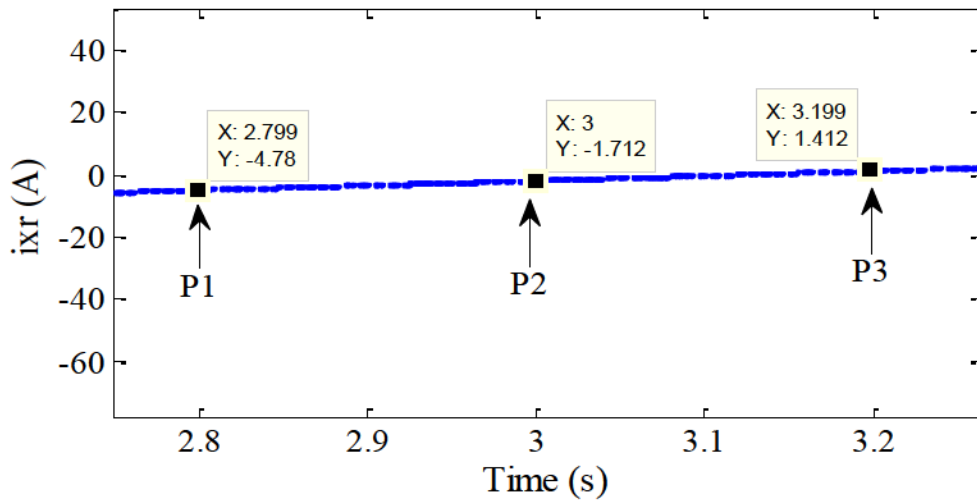


Fig. 5-9. The i_{xr} in 0.4 s when the error is 0.017 rad/s

As we can see in Fig. 5-9, the i_{xr} has slope due to 0.017 rad/s error in ω_{sl} , and by calculating the variation in the samples by (5.8) it is possible to identify the characteristics of i_{xr} as below:

$$\text{Sum} = |P_1 - P_2| + |P_1 - P_3| + |P_2 - P_3| \quad (5.8)$$

If the (sum < 0.01), then $i_{\alpha r}$ is aligned with the d-axis and indicate that the correct ω_{sl} was achieved, and if the (sum > 0.01) then $i_{\alpha r}$ is aligned with the x-axis of an arbitrary reference frame and the incorrect $\hat{\omega}_{sl}$ was achieved. (It is noted that selecting 0.01 that means the P_1 , P_2 and P_3 are reasonably located in the same line).

In Fig. 5-9, by using three different sample of i_{xr} at $t = 2.8$ s, $t = 3$ s and $t = 3.2$ s and using (5.8), the value of sum is

$$\text{sum} = |-4.78 - (-1.712)| + |-4.78 - (1.412)| + |-1.712 - (1.412)| = 12.38 \quad (5.9)$$

Thus:

The sum is not less than 0.01 that means $i_{\alpha r}$ is aligned with x-axis and i_{xr} was obtained. In order to obtain sum < 0.05, a new ω_{sl} should be applied again in (5.5), and the estimation algorithm keeps processing until sum < 0.01 is achieved which indicates that the transformation vector of $i_{\alpha r}$ has been aligned with d-axis of synchronous reference frame and ω_{sl} was achieved.

In addition, as shown in Fig. 5-10, the v_{dr} and v_{qr} which are estimated in synchronous reference frame from conventional control scheme or new control scheme, have to be transferred to stationary $\alpha\beta_r$ reference frame by $\omega_{sl}t$ and then transferred to v_{abc_r} to provide three-phase modulating waveforms. These back and forth transformation between synchronous reference frame, stationary reference frame and three phase reference frame will be applied for whole control strategy for rotor variables in order to control active and reactive power for DFIG.

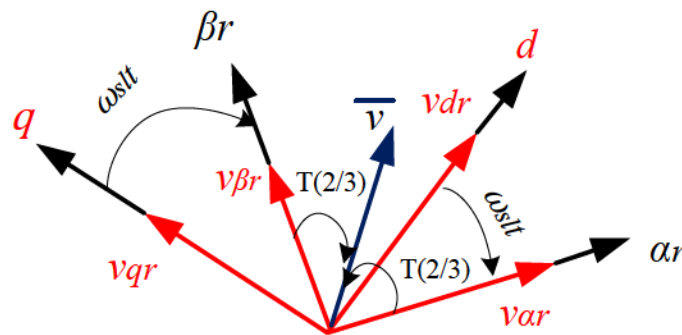


Fig. 5-10. Space vector diagram to transfer v_{dqr} to $v_{\alpha\beta r}$ and then to v_{abc_r}

5.3 Verification of New Position-Sensorless Estimation Scheme

If we use the position encoder's sensor to measure a rotor position θ_r , the slip angular displacement can be computed by

$$\theta_{slip} = \theta_s - \theta_r \quad (5.10)$$

Where θ_s is stator flux position respect to the stator stationary axis. And the θ_r is a position of rotor axis respect to stator stationary axis. The slip angular displacement is required in order to transfer rotor variables from rotor axis to synchronous axis for vector control strategy.

By getting derivative from (5.10), the slip angular frequency can be expressed as

$$\omega_{slip} = (2/P) \omega - \omega_r \quad (5.11)$$

Where,

ω is stator frequency which is equal to $2\pi f_s$, the f_s is grid frequency, and ω_r is rotor mechanical speed and P is a number of poles.

The accuracy of new scheme is investigated with the help of the example in Sub-section 5.3.1. This Sub-section verifies the new sensorless estimation scheme by comparing between ω_{sl} and ω_{slip} . The ω_{sl} is slip angular frequency which is estimated by the new scheme.

5.3.1 Example

The parameters of the induction machine considered in this example are given in Table 3-1.

As indicated in Fig. 5-11, the operation of the rotor speed for $0 \leq t \leq 14$ will be define as bellow ;

$\omega_r = 188.3$ rad/s between $0 \leq t \leq 3$ s, $\omega_r = 194.1$ rad/s between $3 \leq t \leq 6$ s, $\omega_r = 198$ rad/s between $6 \leq t \leq 10$ s and decreased to $\omega_r = 190.3$ at $t \geq 10$ s.

The slip angular frequency can be computed for each input mechanical torque through (5.12) to (5.14). The synchronous speed is $\omega_s = (2/P) \omega = 188.4$ rad/s, and the rotor speed ω_r is derived from Fig. 5-11.

Thus:

For $3 \text{ s} \leq t \leq 6 \text{ s}$, $T_m = 150 \text{ Nm}$

$$\omega_{slip} = 188.4 - 194.1 = -5.7 \text{ rad/s} \quad (5.12)$$

For $6 \text{ s} \leq t \leq 10 \text{ s}$, $T_m = 250 \text{ Nm}$

$$\omega_{slip} = 188.4 - 198 = -9.6 \text{ rad/s} \quad (5.13)$$

For $t \geq 10 \text{ s}$, $T_m = 50 \text{ Nm}$

$$\omega_{slip} = 188.4 - 190.3 = -1.9 \text{ rad/s} \quad (5.14)$$

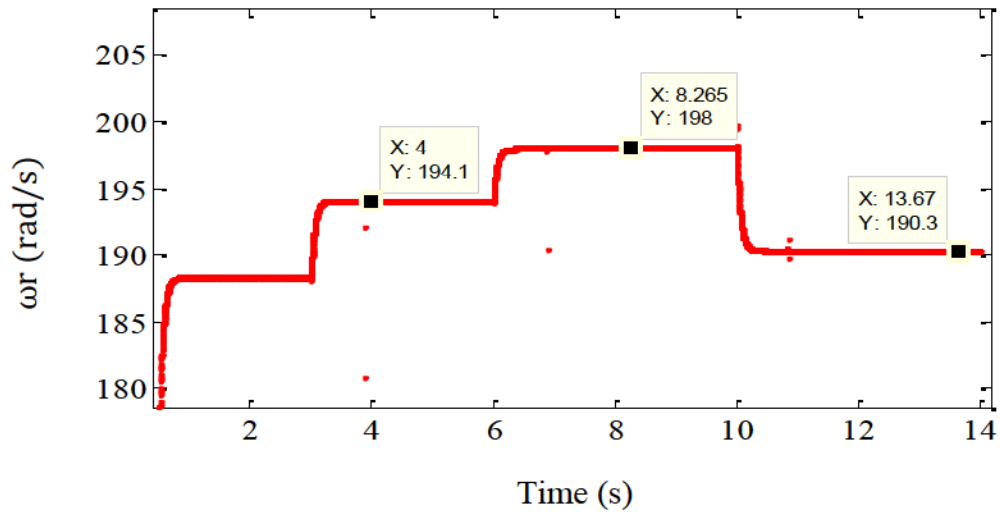


Fig. 5-11. Rotor speed

Those computations were based on using incremental position sensor. And the simulation result of ω_{slip} for different input mechanical torque is shown in Fig. 5-12.

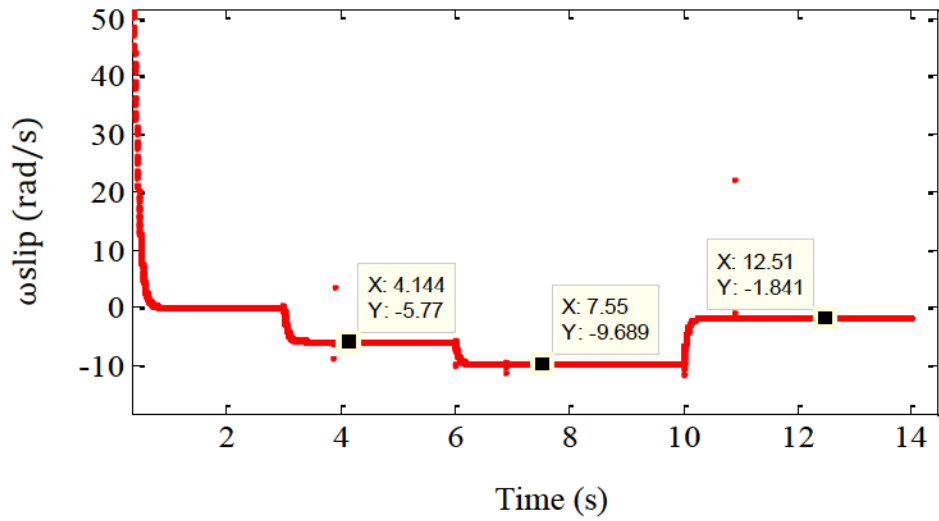


Fig. 5-12. Slip angular frequency ω_{slip}

In order to estimate slip angular frequency in new scheme the rotor current will be transferred in stationary rotor axis to provide $i_{\alpha\beta r}$, the stationary rotor current is shown in Fig. 5-13.

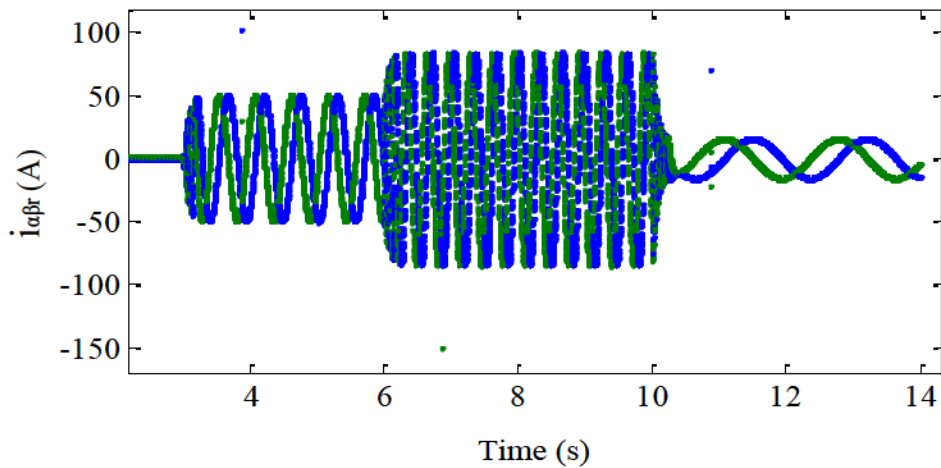


Fig. 5-13. Stationary rotor current ($i_{\alpha\beta r}$)

Fig. 5-14 shows the sampling process and estimation process to obtain correct ω_{sl} in 0.8 s. Fig. 5-14 only shows the process of estimation when the rotor speed increase to $\omega_r = 194.1$ rad/s between 3 s

$\leq t \leq 6$ s. The process of estimation is the same as Sub-section 5.2.1. By taking six samples from $i_{\alpha\beta r}$ at t_1 , t_2 and t_3 and by applying different ω_{sl} in (5.18) the different amount of i_{dr} will be achieved and only one ω_{sl} makes the P_1 , P_2 and P_3 are going in the same line and as expressed in (5.8) and if the (sum < 0.01), then $i_{\alpha r}$ is aligned with the d-axis and indicate that the correct ω_{sl} was obtained.

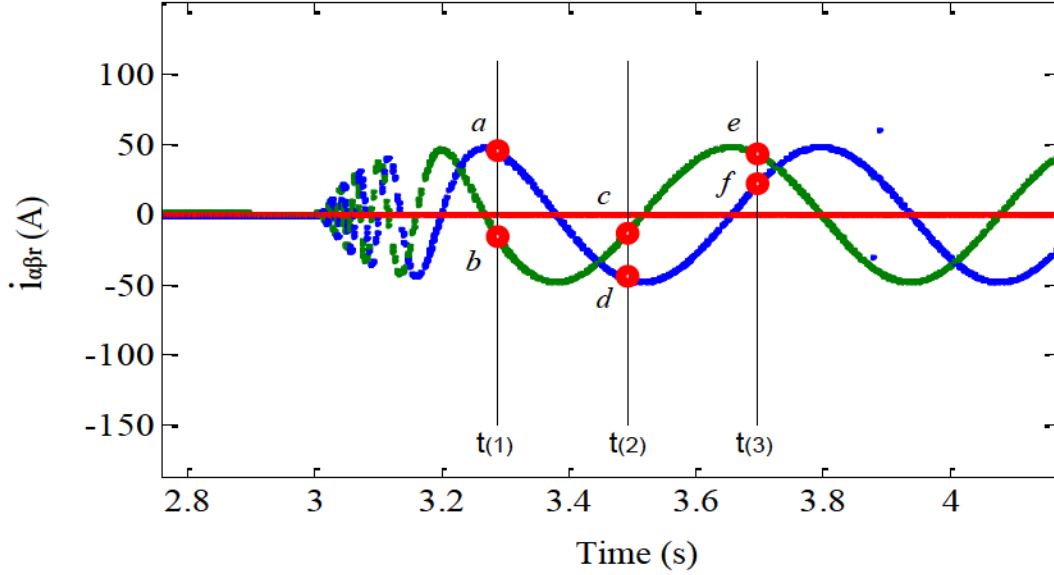


Fig. 5-14. Take the sample from stationary rotor current

$$\begin{bmatrix} i_{dr} \\ i_{qr} \end{bmatrix} = \begin{bmatrix} \cos(\omega_{sl}t) & \sin(\omega_{sl}t) \\ -\sin(\omega_{sl}t) & \cos(\omega_{sl}t) \end{bmatrix} \cdot \begin{bmatrix} i_{\alpha r} \\ i_{\beta r} \end{bmatrix} = \begin{cases} i_{\alpha r} = I_m \cos(\omega_{slip}t) \\ i_{\beta r} = I_m \sin(\omega_{slip}t) \end{cases} \quad (5.15)$$

$$i_{dr} = i_{\alpha r} \cdot \cos(\omega_{sl}t) + i_{\beta r} \cdot \sin(\omega_{sl}t) \quad (5.16)$$

Where, $\omega_{sl} = k_1 : 0.1 : k_2$

$$i_{dr}(t_1) = a \cos(\omega_{sl}t_1) + b \sin(\omega_{sl}t_1) = P_1 \quad (5.17)$$

$$i_{dr}(t_2) = d \cos(\omega_{sl}t_2) + c \sin(\omega_{sl}t_2) = P_2 \quad (5.18)$$

$$i_{dr}(t_3) = f \cos(\omega_{sl}t_3) + e \sin(\omega_{sl}t_3) = P_3 \quad (5.19)$$

$$\text{Sum} = |P_1 - P_2| + |P_1 - P_3| + |P_2 - P_3| \quad (5.20)$$

As shown in Fig. 5-15, the $i_{\alpha\beta r}$ is changed due to change in input mechanical torque and ω_{sl} is achieved by analyzing the variation of rotor current in 0.8 s for different input mechanical torque.

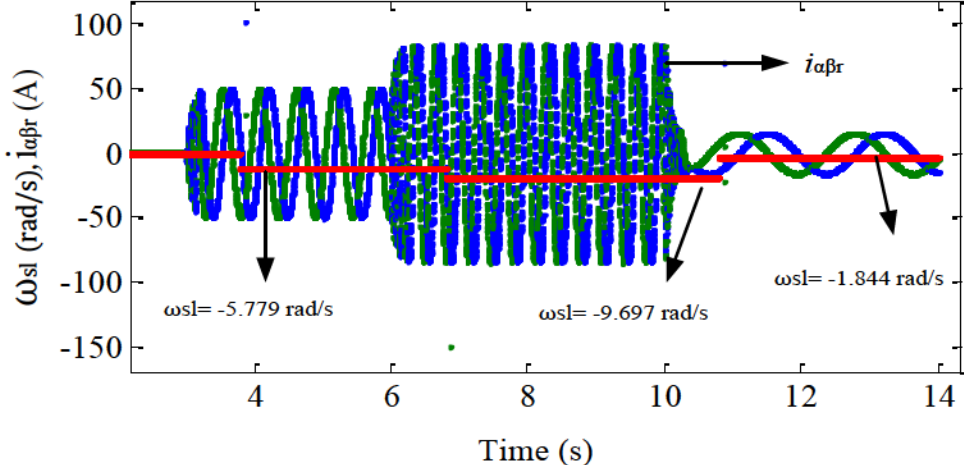


Fig. 5-15. Slip angular frequency and stationary rotor current

Once the correct ω_{sl} is estimated, the $i_{\alpha\beta r}$ will be aligned with d-q synchronous reference frame after transformation and provide $i_{dq r}$. Fig. 5-16 shows that the correct ω_{sl} is estimated caused the i_{qr} aligned with q-axis synchronous frame and is going to be constant, this alignment will be obtained after 0.8 s for any change in rotor current.

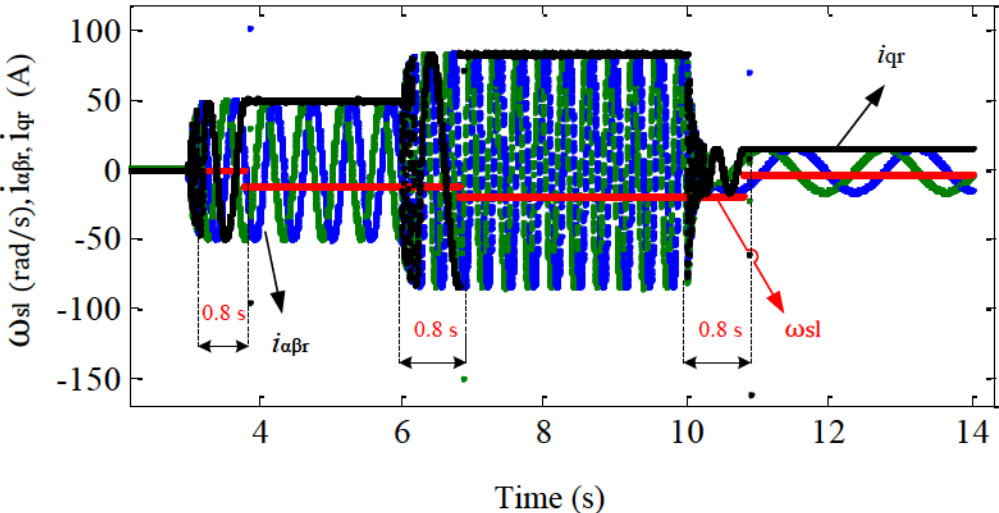


Fig. 5-16. Slip angular frequency, stationary rotor current and q-axis rotor current

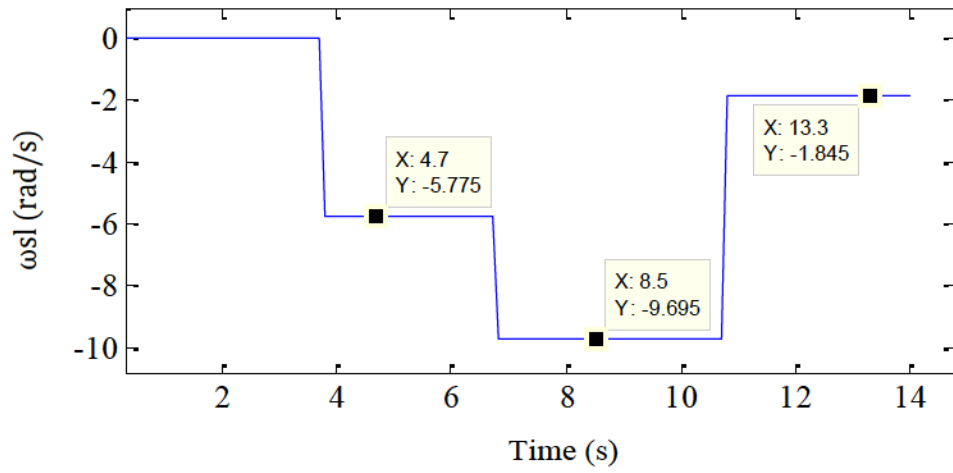


Fig. 5-17. Slip angular frequency ω_{sl} estimated in new scheme

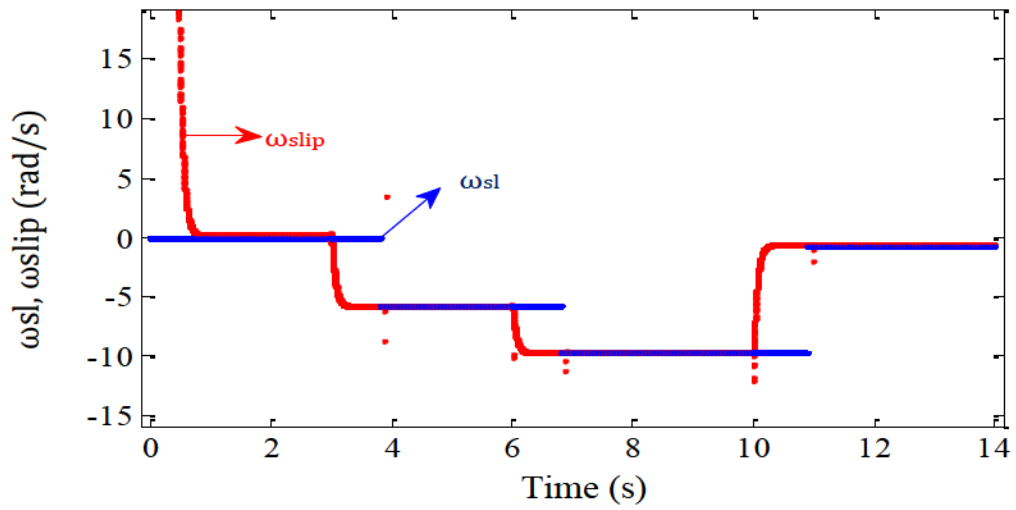


Fig. 5-18 (a). Slip angular frequency ω_{slip} and ω_{sl}

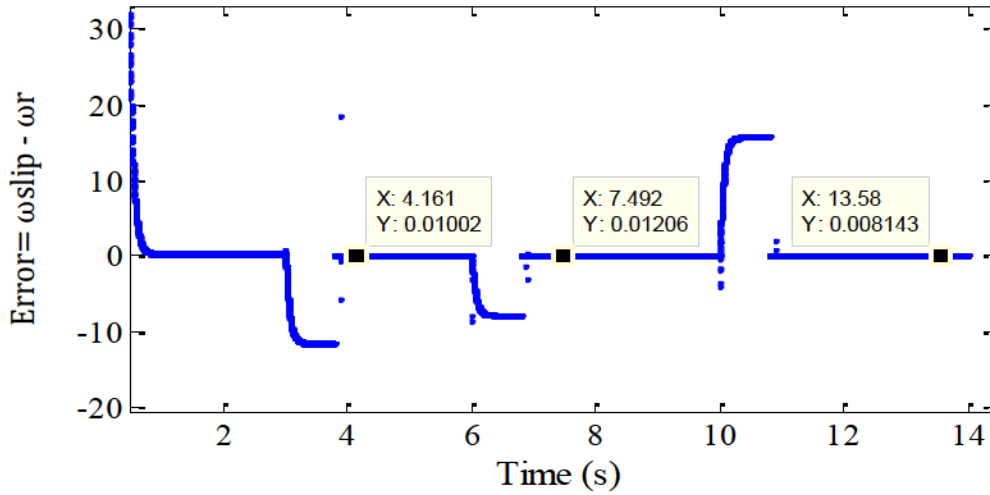


Fig. 5-18 (b). Error between ω_{slip} and ω_{sl}

Fig. 5-17 shows the slip angular frequency for different input mechanical torque that was estimated by position-sensorless estimation scheme. The value of slip angular frequency in Fig. 5-17 and Fig. 5-12 has the same amount as shown in Fig. 5-18(a). Fig. 5-18(b) shows the error between ω_{slip} and ω_{sl} when the algorithm is applied to the control system to estimate the slip angular frequency, and this indicates that, the new position-sensorless scheme is able to properly estimate the slip angular frequency with new algorithm.

5.4 Estimation of Slip angular frequency with effect of Rotor Initial position in New Position-Sensorless Scheme

Since the new position-sensorless scheme is able to estimate the slip angular frequency by analyzing variation of rotor current, it is possible to estimate the slip angular frequency when the initial rotor position is effected to the machine. The effect of initial rotor position makes the shift in the phase of rotor currents therefore the position-sensorless algorithm will estimate the slip angular frequency according to the method in the Sub-section 5.2.1

As shown in Fig. 5-19, i_{ar1} is a phase “a” of the rotor current when the initial rotor position at $t = 0$ s is 0 degree, and i_{ar2} is a phase “a” of the rotor current when the initial rotor position at $t = 0$ s is 57.32 degree. The slip angular frequency for i_{ar1} is $\omega_{sl1} = -5.68$ rad/s and for i_{ar2} is $\omega_{sl2} = -4.68$ rad/s, the result of both conditions (with and without initial rotor position) is indicated that the effect of initial rotor position makes different consequences in slip angular frequency estimation which is seen in Fig. 5-19.

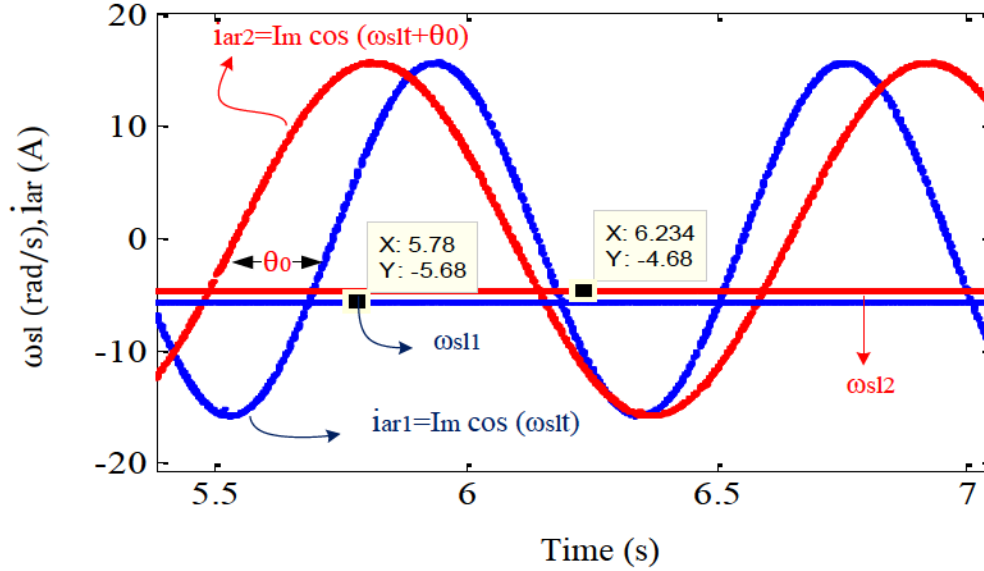


Fig. 5-19. Slip angular frequency ω_{sl} and phase “a” of rotor current

5.5 Simulation Result for operation of DFIG by applying Position-Sensorless estimation and Speed Control Strategy

In Chapter 4 a new speed control strategy was investigated for wound rotor induction machine, and in this Chapter 5, a new position-sensorless algorithm has been developed

In this Section the control of the doubly fed induction generator is investigated when these two new schemes are applied to the system. The simulation result shows the stability of the system when operated with these schemes.

The parameters of the induction machine considered in this Section are given in Table 3-1.

In the simulation depicted in Figs. 5-20 and 5-21, it is assumed the input mechanical torque applied to the wind turbine is $T_m = 50$ Nm at $t = 3$ s. At this time the rotor axis (α_r) is made to change its position due to change in slip frequency. As shown in Fig. 5-20, the position-sensorless algorithm starts processing to estimate a new ω_{sl} from $t = 3$ s to $t = 3.8$ s (0.3 s for the transient to pass, 0.4 s for sampling and 0.1 s for slip frequency estimation). During the time between 3 s and 3.8 s, the rotor q-axis current changes its alignment and it fluctuates in arbitrary reference frame and this is seen in Fig. 5-20.

A new ω_{sl} is estimated at $t = 3.8$ s and it causes the i_{qr} to take on DC value at $t = 3.8$ s, and the i_{qr1} and ω_{sl1} are derived from Fig. 5-20 at $t = 3.8$ s.

Once the i_{qr1} and ω_{sl1} are obtained, the v_{qr} can be injected to the rotor circuit to regulate the rotor speed, the v_{qr} is applied to the rotor circuit at $t = 5$ s in order to control the rotor speed. It is to be noted that during the time between 3 and 5 s the v_{qr} is not injected into the rotor circuit, therefore the rotor speed is increased corresponding to the input mechanical torque.

The v_{qr} for position-sensorless estimation method in super synchronous mode is expressed as:

$$v_{qr} = k * (-\omega_{sl} L_r i_{qr}) \quad (5.21)$$

As shown in Fig. 5-21, when the v_{qr1} is applied to the rotor circuit, the rotor speed is regulated to desired speed at $t = 5$ s. The i_{qr} once again goes out of alignment and it vary in arbitrary reference frame due to injecting v_{qr1} between $t = 5$ s to $t = 5.8$ s. During that time the slip angular frequency estimation algorithm start processing to find a new ω_{sl} . In Fig. 5-20, the ω_{sl2} is obtained at $t = 5.8$ s and it causes the i_{qr2} to be a DC value. The i_{qr2} and ω_{sl2} will be used for the other rotor speed regulation, the v_{qr2} is applied to the rotor circuit at $t = 7$ s in order to control the rotor speed, the rotor speed is regulated to desired speed at $t = 7$ s. The i_{qr} once again goes out of alignment and it vary in arbitrary reference frame due to injecting v_{qr2} between $t = 7$ s to $t = 7.8$ s and during that time the slip angular frequency estimation algorithm start processing to find a new ω_{sl} . In Fig. 5-20, the ω_{sl3} is obtained at $t = 7.8$ s and it causes the i_{qr3} to be a DC value. The i_{qr3} and ω_{sl3} will be used for the other rotor speed regulation, the v_{qr3} is applied to the rotor circuit at $t = 9$ s in order to control the rotor speed, the rotor speed is regulated to desired speed at $t = 9$ s. The i_{qr} once again goes out of alignment and it vary in arbitrary reference frame due to injecting v_{qr3} between $t = 9$ s to $t = 9.8$ s and during that time the slip angular frequency estimation algorithm start processing to find a new ω_{sl} . In Fig. 5-20, the ω_{sl4} is obtained at $t = 9.8$ s and it causes the i_{qr4} to be a DC value. The i_{qr4} and ω_{sl4} will be used for the other rotor speed regulation, the v_{qr4} is applied to the rotor circuit at $t = 11$ s in order to control the rotor speed, the rotor speed is regulated to desired speed at $t = 11$ s. The i_{qr} once again goes out of alignment and it vary in arbitrary reference frame due to injecting v_{qr4} between $t = 11$ s to $t = 11.8$ s and during that time the slip angular frequency estimation algorithm start processing to find a new ω_{sl} . In Fig. 5-20, the ω_{sl5} is obtained at $t = 11.8$ s and it causes the i_{qr5} to be a DC value and as shown in Fig. 5-21, it is assumed the system at $t = 11$ s is settled in desired speed and operated in stability condition.

As shown in these simulations the system stabilizes for different input mechanical torque or by applying different v_{qr} .

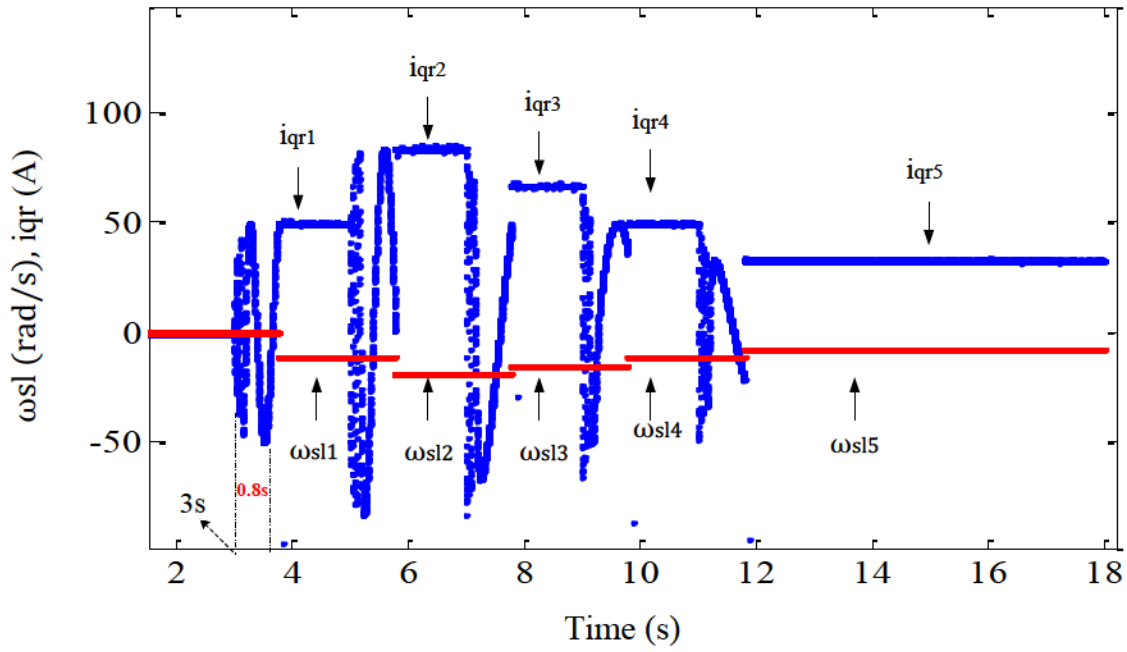


Fig. 5-20. q-axis rotor current and slip frequency ω_{slip} in new scheme

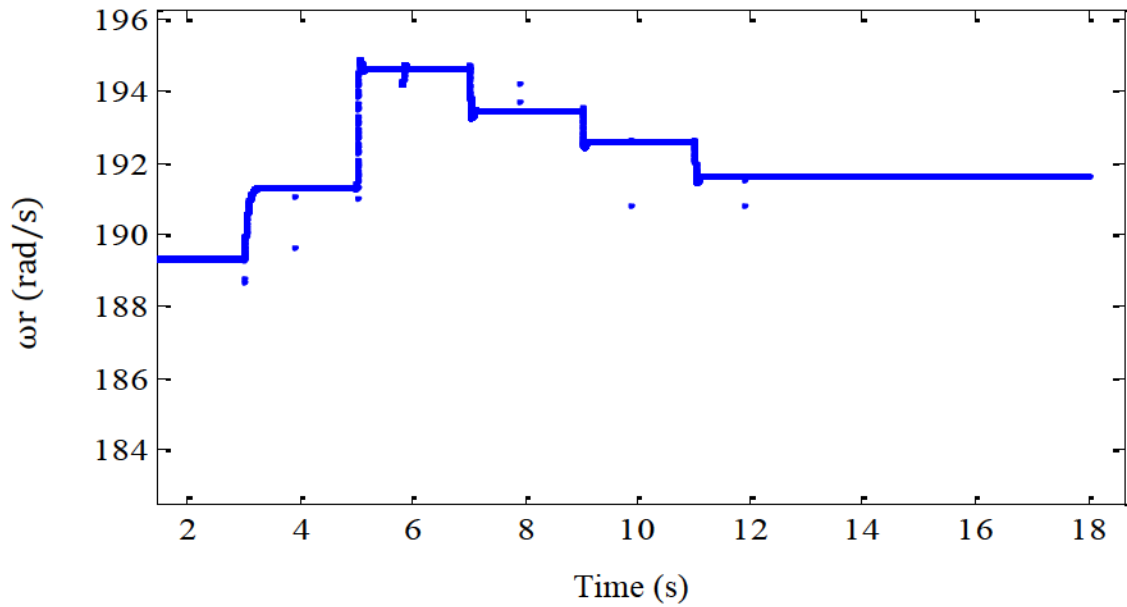


Fig. 5-21. Control rotor speed in new scheme

The result of the above simulations shows that, this new scheme is able to estimate the slip angular frequency especially when the machine speed operates close to synchronous speed and the algorithm can be started without the knowledge of initial rotor position.

The result of the simulations shows the accuracy of both new control schemes in this thesis for doubly fed induction machine based wind energy conversion system.

Chapter 6

Conclusion

The main purpose of this thesis is to simplify and improve control scheme for Doubly Fed Induction Machine based wind energy conversion system by applying new schemes of position-sensorless estimation and speed control for DFIG to reduce the cost and improve reliability.

Chapter 1 and 2 provide extensive background knowledge on the wind energy market, turbine technology, and energy conversion.

In Chapter 3, the operation of the doubly fed induction generator DFIG was discussed. The steady-state operation for the DFIG was introduced and analyzed in detail. The simulation result uses a DFIG model in d-q axis reference frame to obtain characteristics under general d-q conditions in the stator flux oriented frame. Chapter 3 illustrated that the doubly fed induction generator based wind turbine achieved decoupled control of active and reactive powers independently through PI controller design. The steady-state and dynamic performance was investigated by computer simulations and power balance calculations in the steady-state.

In Chapter 4, through simulation it has been shown that a new speed control scheme is able to control the rotor speed to find maximum power in wind energy conversion system. This new scheme does not use the q-axis rotor current as reference to regulate the rotor speed, therefore the complexity of PI controller design can be reduced. The maximum power point can be extracted under wind fluctuations due to use of HCS algorithm and new speed control scheme for doubly fed induction generator.

In Chapter 5, the estimation of slip angular frequency was investigated based on position-sensorless estimation method. Through the simulation results, this new scheme illustrated that it is able to estimate the slip angular frequency for different operating conditions. The algorithm can be started without the knowledge of the initial rotor position. The proposed method of computation rotor current makes the estimation process independent of critical machine parameters.

Simulation results in chapter 5 indicates that the new method is appropriate for vector control of the DFIG to estimate slip angular frequency for different operating conditions.

Finally in Chapter 5, it shown that the slip angular frequency estimation scheme works well with the speed control scheme developed in Chapter 4 and the composite strategy keeps the system stable and operating reliably.

References

- [1] Renewable Energy Policy Network for the 21st Century (REN21), Renewable Global Status Report 2009 Update, available at www.ren21.net
- [2] Global Wind Energy Council (GWEC), Global Wind 2009 Report, available at www.gwec.net
- [3] P. Gipe, "Design as if people matter: Aesthetic guidelines for the wind industry," American Wind Energy Associates Conference, March 1995, available at www.wind-works.org.
- [4] M. Wolsink, M. Sprengers, A. Keuper, T.H. Pedersen, and C.A. Westra, "Annoyance from wind turbine noise on sixteen sites in three counties," Proc. European Community Wind Energy Conf., Lubeck- Travemunde, Germany, March 1993.
- [5] K. Bevenger. Bird interactions with utility structures: collision and electrocution, causes and mitigating measures. *Ibis* 136: 412 - 425. 1994, October 1994.
- [6] B. Wu, Y. Lang, N. Zargari, and S. Kouro, "*Power Conversion and Control of Wind Energy Systems*," Wiley & IEEE Press, ISBN 978-0-470-59365-3, winter 2012.
- [7] O. A. Lara, N. Jenkins, J. Ekanayake. P. Cartwright and M. Hughes, "*Wind Energy Generation Modeling and Control*," John Wiley and Sons, ISBN 978-0-470-71433-1, 2009.
- [8] E. Hau, "*Wind Turbines: Fundamentals, Technologies, Application, Economics*," ISBN 3-540-57064-0, 2nd edition, Springer 2005.
- [9] R. Datta and V. T. Ranganathan, "Variable-speed wind power generation using doubly fed wound rotor induction-A comparison with alternative schemes," *IEEE Trans. Energy Conversion*, vol. 17, no. 3, pp. 414 - 421, Sept 2002.
- [10] S. Muller, M. Deicke, and R. W. De Doncker, "Doubly fed Induction generator system for wind turbines," *IEEE Ind. Appl.*, vol. 17, no. 1, pp. 26 - 33, May/June 2002.
- [11] R. Datta and V. T. Ranganathan, "A method of tracking the peak power points for a variable speed wind energy conversion system," *IEEE Trans. Energy Conversion*, vol. 18, no. 1, pp. 163 - 168, March 2003.
- [12] E. Koutroulis and K. Kalaitzakis, "Design of a Maximum Power Tracking System for Wind Energy Conversion Applications," *IEEE Trans. Power Electronics*, vol. 53, no. 2, pp. 486 - 494, April 2006.

- [13] N. Ullah, K. Bhattacharya, T. Thiringer, "Wind Farms as Reactive Power Ancillary Service Providers- Technical and Economic Issues," *IEEE Trans. Energy Conversion*, vol. 24, no. 3, pp. 661 - 672, Sept 2009.
- [14] P. Krause, O. Wasynczuk, and S. D. Sudhoff, "*Analysis of Electric Machinery and Drive System*," ISBN 0-471-14326-X, Hoboken, NJ: Wiley, 2002.
- [15] S. Muller, M. Deicke and R. W. De Doncker, "Doubly fed Induction generator system for wind turbines," *IEEE Ind. Appl.*, vol. 17, no. 1, pp. 26 - 33, May/Jun 2002.
- [16] H. Akagi and H. Sato, "Control and performance of doubly fed induction machine intended for a flywheel energy storage system," *IEEE Trans. Power Electronics*, vol. 17, no. 1, pp. 109 - 116, Jan 2002.
- [17] E. Tremblay, S. Atayde, and A. Chandra, "Comparative Study of Control Strategies for the Doubly Fed Induction Generator in Wind Energy Conversion System," *IEEE Trans. Power Electronics*, vol. 2, no. 3, pp. 288 - 299, July 2011.
- [18] G. Tapia, G. Santamaria, M. Telleria and A. Susperregui, "Methodology for Smooth Connection of Doubly Fed Induction Generators to the Grid," *IEEE Trans. Energy Conversion*, vol. 24, no. 4, pp. 959 - 971, December 2009.
- [19] N. Idris, A. Yatim, "An Improved Stator Flux Estimation in Steady-State Operation for Direct Torque Control of Induction Machines," *IEEE Trans. Ind. Appl.*, vol. 38, no. 1, pp. 110 - 116, Jan/Feb 2002.
- [20] M. Ho Shin, D. Seok Hyun, "An Improved Stator Flux Estimation for Speed Sensorless Stator Flux Orientation Control of Induction Motors," *IEEE Trans. Power Electronics*, vol. 15, no. 2, pp. 312 - 318, March 2000.
- [21] Q. Wang and L.C. Chang, "An intelligent maximum power extraction algorithm for inverter-based variable speed wind turbine systems," *IEEE Trans. Power Electronics*, vol. 19, no. 5, pp. 1242 - 1249, Sept 2004.
- [22] J. D. Roberts, "Extremum or hill-climbing regulation: a statistical theory involving lags, disturbances and noise," *IEEE Proc*, vol. 112, no. 1, January 1965.
- [23] S. Kazmi, H. Goto, H. Guo and O. Ichinokura, "A Novel Algorithm for Fast and Efficient Speed-Sensorless Maximum Power Point Tracking in Wind Energy Conversion System," *IEEE Trans. Power Electronics*, vol. 58, no. 1, pp. 29 - 36, Jan 2011.

- [24] B. Shen, B. Mwinyiwiwa, Y. Zhang and B. T. Ooi, "Sensorless Maximum Power Point Tracking of Wind by DFIG Using Rotor Position Phase Lock Loop (PLL)," *IEEE Trans. Power Electronics*, vol. 24, no. 4, pp. 942 - 951, April 2009.
- [25] Z. Wang, G. Li, Y. Sun and B. T. Ooi, "Effect of Erroneous Position Measurements in Vector-Controlled Doubly Fed Induction Generator," *IEEE Trans. Energy Conversion*, vol. 25, no. 1, pp. 59 - 69, March 2010.
- [26] R. Datta and V. T. Ranganathan, "A simple position-sensorless algorithm for rotor-side field-oriented control of wound-rotor induction machine," *IEEE Trans. Ind. Electron.* vol. 48, no. 4, pp. 786 - 793, Aug 2001.
- [27] R. Peña, R. Cárdenas, J. Proboste, G. Asher, and J. Clare, "Sensorless control of doubly-fed induction generators using a rotor-current-based MRAS observer," *IEEE Trans. Ind. Electron.* vol. 55, no. 1, pp. 330 - 339, Jan 2008.
- [28] L. Morel, H. Godfroid, A. Mirzaian, and J. M. Kauffmann, "Double-fed induction machine: converter optimization and field oriented control without position sensor," *Proc. Inst. Elect. Eng.* vol. 145, no. 4, pp. 360 - 368, July 1998.